Ore Geology Reviews 101 (2018) 819–838

Contents lists available at ScienceDirect

Ore Geology Reviews

journal homepage: www.elsevier.com/locate/oregeorev

A pilot study to test the reliability of the ERT method in the identification of mixed sulphides bearing dykes: The example of Sidi Flah mine (Anti-Atlas, Morocco)

Stefano Bernardinetti[a,b], Diego Pieruccioni[c,*], Enrico Mugnaioli[d,e], Franco Maria Talarico[e,f], Marilena Trotta[b], Aziz Harroud[g], Emanuele Tufarolo[b,f]

[a] University of Cagliari - Chemical and Earth Sciences Department, Via Trentino 51, 09127 Cagliari, Italy
[b] University of Siena - CGT Center for GeoTechnologies, Via Vetri Vecchi 34, 52027 San Giovanni Valdarno, Italy
[c] University of Pisa - Earth Sciences Department, Via S. Maria 53, 56126 Pisa, Italy
[d] Center for Nanotechnology Innovation@NEST - Istituto Italiano di Tecnologia, Piazza San Silvestro 12, 56127 Pisa, Italy
[e] PetroLogicSynergy (PLS) srl spin-off - University of Siena, Via Vezzosi 15, 52300 Arezzo, Italy
[f] University of Siena - Department of Environment, Earth and Physical Sciences, Via Laterina 8, 53100 Siena, Italy
[g] Société Marocaine de Géo-Technologies (SMG) srl spin-off - University of Siena, Hay Asgoune Amizmiz 46, Marrakech, Morocco

ARTICLE INFO

Keywords:
ERT
Structural investigation
Mixed sulphides
Petrographical analyses
Anti-Atlas
Morocco

ABSTRACT

A multidisciplinary study, comprising geological, petrographical and geophysical methods, was carried out for the identification and the geometrical and volumetric assess of the main mineralized bodies (mixed sulphides, Zn-Pb and Fe-Cu) in the area of the Anti-Atlas chain, located at SW of the town of Sidi Flah (Ouarzazate, Morocco). The initial phase of exploration involved an extensive fieldwork (structural investigations and sampling) and a detailed survey for verifying the effectiveness and reliability of the Electrical Resistivity Method (ERT). Geological fieldworks and laboratory analyses played a fundamental role in identifying the resistivity anomalies and constraining tomographic results. Main issues we focused on are: i) mineralized bodies imaging according to the electrodic step; ii) consistency with geometry of mineralized bodies; iii) contrast of electrical resistivity between mineralized dykes and host rocks; iv) possible correlations between the type and amount of sulphides and electrical resistivity.

1. Introduction

The Sidi Flah mine is located in the Skoura mining district in Eastern Anti-Atlas, SE of Morocco, on the northern side of the West African Craton (WAC). This area is characterized by Neoproterozoic rocks, metamorphosed and strongly deformed during the Pan-African Orogenesis, and later covered by younger alluvial sediments of Pleistocene age. This mining district hosts several kinds of ore deposits (Rezeau et al., 2014 and reference therein), which range from Paleoproterozoic to Ordovician age. The economic importance of the area has led to numerous geological and geophysical activities in order to understand its geological evolution and hence discover new ore deposits (Barodi et al., 1998; Abia et al., 1999, 2003; Benssaou and Hamoumi, 1999; Cheilletz et al., 2002; Gasquet et al., 2005; Rezeau et al., 2014 and reference therein).

Among the geophysical methods used for the prospection of mineral deposits, the electrical ones are rather widespread in several geological contexts (e.g. Loke et al., 2013 and reference therein). In particular, the induced-polarization method (IP), often coupled to the Electrical Resistivity Method (ERT), can be nowadays considered part of a quite consolidated protocol (Grant and West, 1965; Bhattacharya and Patra, 1968; Sumner, 1976; Bertin and Loeb, 1976; Koefoed, 1979; Wong and Strangway, 1981; Parasnis, 1986; Dahlin et al., 2002; Evrad et al., 2005; Dahlin and Zhou, 2006; Jochymczyk et al., 2006; Magnusson et al., 2010; Morgan, 2012; Alilou et al., 2014; Kumar et al., 2016; Tavakoli et al., 2016 and reference therein). Conversely, ERT is rarely used alone (e.g. Legault et al., 2008; Mele et al., 2013). Nevertheless, this geoelectrical method is very economical in its implementation and requires a significant shorter time for data acquisition when compared to IP.

Therefore, we decided to test the possibility of locating and discriminating different types of mixed sulphide mineralized bodies based on their resistivity values.

Later, the ERT surveys have been integrated using geological-structural surveys and mineralogical and petrographical analyses in

* Corresponding author.
E-mail address: diego.pieruccioni@dst.unipi.it (D. Pieruccioni).

https://doi.org/10.1016/j.oregeorev.2018.08.028
Received 24 February 2018; Received in revised form 31 July 2018; Accepted 21 August 2018
Available online 23 August 2018
0169-1368/

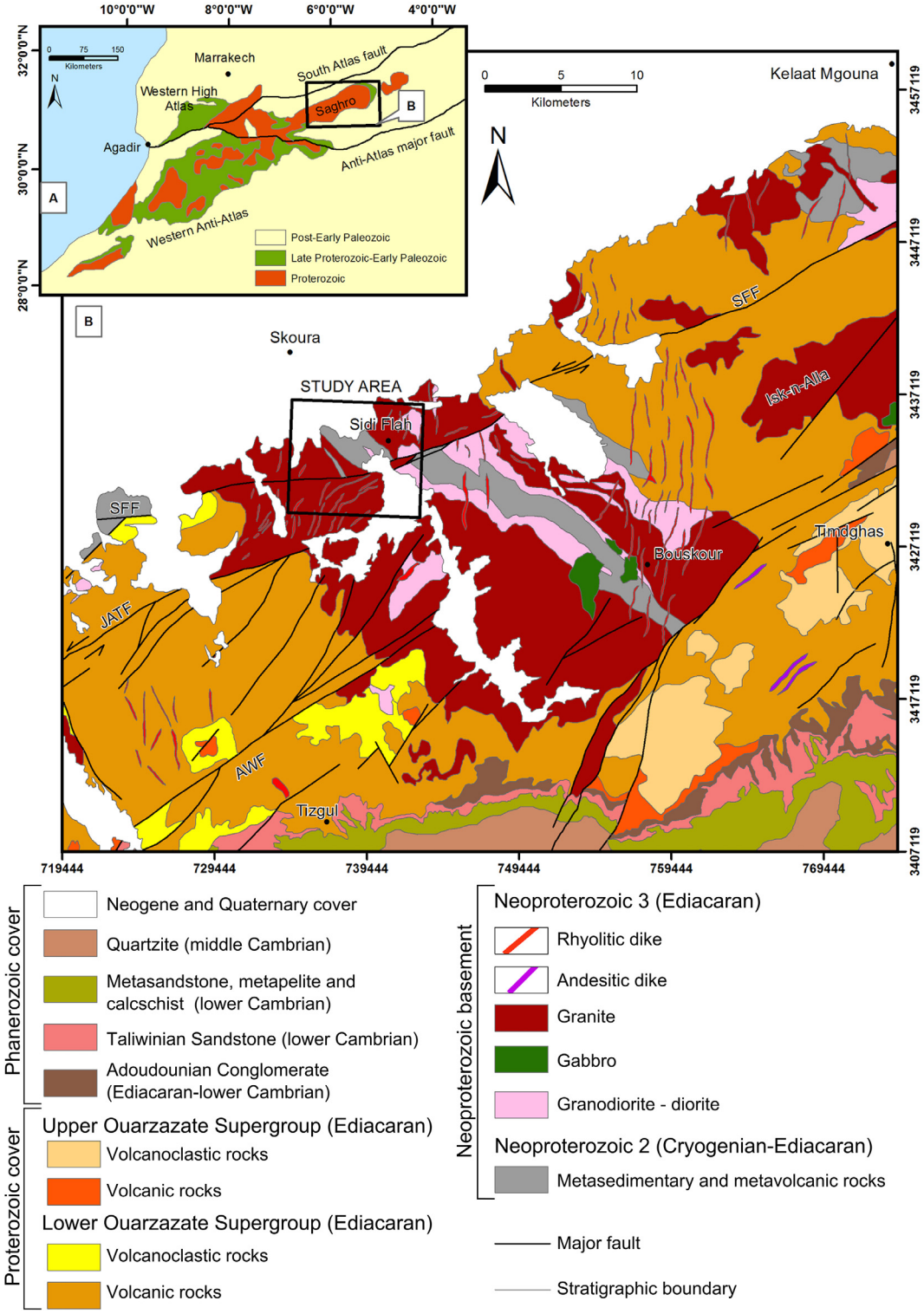

Fig. 1. (a) Simplified structural map of High- and Anti-Atlas Chain. In orange they are reported the Moroccan inliers with Proterozoic age; in green the Late Proterozoic-Early Paleozoic rocks; in light yellow the Phanerozoic cover rocks (modified after Fekkak et al., 2003). (b) Simplified geological map of the Jebel Saghro inlier showing the studied area (from Walsh et al. 2012 modified). Abbreviations include: SFF - Sidi Flah fault; JATF - Jebel Azouguiygh-n-Tazoult fault; AWF - Awzou-n-Wallows fault. (Datum: WGS84; Projection: Transverse Mercator, Zone 29 North). (For interpretation of the references to colour in this figure legend, the reader is referred to the web version of this article.)

order to interpret the 2D electrical tomographic data. The combination of all these methods allowed us to understand the structural setting of the ore deposit, the types of sulphide mineralization and the depth of their occurrence within the host rock of the Skoura mining district.

2. Geologic setting

2.1. General geology

The Sidi Flah mixed sulphides deposit is located at southeast of

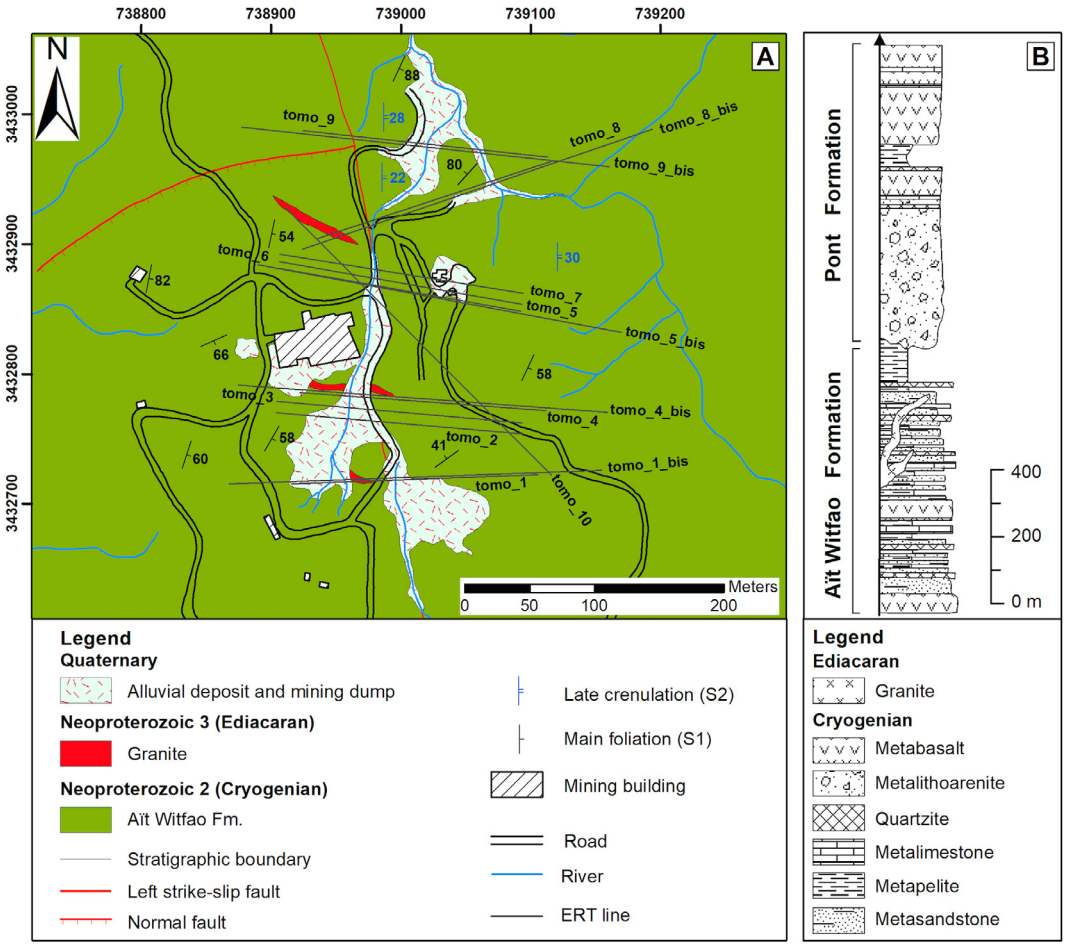

Fig. 2. (a) Geological map of Sidi Flah mining area with the location of ERT lines. (b) Stratigraphic column of Sidi Flah area (modified after Fekkak et al., 2003). (Datum: WGS84; Projection: Transverse Mercator, Zone 29 North).

Skoura village, on the northern side of the Saghro massif, which constitutes the Anti-Atlas orogenic belt (AA) of Morocco. The AA consists of different Proterozoic terrains, which derived from the amalgamation of Gondwana (e.g. Villeneuve and Cornée, 1994; Hefferan et al., 2000, 2002; Michard et al., 2008), exposed as inliers in Phanerozoic formations (Fig. 1a). It can be subdivided into three major structural domains following the early works of Choubert (1947, 1952): i) western AA is localized at south of the Anti-Atlas major fault (AAMF); ii) central AA occurs along the AAMF; iii) eastern AA occurs at north of the AAMF (Fig. 1a). In the western domain, the inliers include Paleoproterozoic granites, gneiss and amphibolites dated around 2 Ga and overlain by gently folded Neoproterozoic clastic sedimentary rocks, all of which were intruded by Pan-African granites between 625 and 550 Ma (Charlot, 1976; Aït Malek et al., 1998; Thomas et al., 2002; Walsh et al., 2002, 2012). The Paleoproterozoic rocks of the western domain belong to the northwest border of the West African Craton (WAC), whereas the central and eastern domains are parts of the Pan-African mobile belt (e.g. Ennih and Liégeois, 2001, 2008; Bouougri, 2003; Gasquet et al., 2008; Nance et al., 2008). The central Anti-Atlas corresponds to a suture zone defined by an ophiolitic complexes (Leblanc and Lancelot, 1980; Shermerhorn et al., 1986; El Boukhari et al., 1992) which belonged to an oceanic basin that was subducted to the north (Saquaque et al., 1989; Hefferan et al., 2002). Ophiolite-related acid volcanic rocks are dated between 743 and 663 Ma (Thomas et al., 2002) and an ophiolitic plagiogranite is dated at 760 Ma (Admou et al., 2002), which constrains the age of the ocean basin. The eastern Anti-Atlas is divided into two massifs, the Saghro and the Ougnat, both consisting of Neoproterozoic terrains exposed within a Phanerozoic cover. The Neoproterozoic terrains of the Saghro Group was deformed and metamorphosed from low- to very-low-green schist facies assemblages during Pan-African orogenesis (Ighid et al., 1989; Saquaque et al., 1992; Ouguir et al., 1996; Fekkak et al., 2001; Thomas et al., 2004; Stone et al., 2008; Benziane et al., 2008; Walsh et al., 2008a; Harrison et al., 2008) and the deformation structures can be connected with two main tectono-metamorphic regional events defined by Leblanc and Lancelot (1980) B1 and B2. The first event (B1) was collisional and generated strong folding and the ophiolite emplacement. The second event (B2) caused moderate shortening and tilting. These two events were previously dated at 685 ± 15 Ma (Clauer, 1974) and 615 ± 12 Ma (Ducrot, 1979). Recent U–Pb ages date B1 around 660 Ma, and B2 between 586 and 575 Ma (Thomas et al., 2002). These two events are used to subdivide the Neoproterozoic Eonothem into three regional sequences: i) the folded lower Precambrian 2 (LP-2) (pre-B1); ii) the unconformably overlying upper Precambrian 2 (UP-2) (pre-B2); iii) the Precambrian 3 (P-3) (post-B2). Considering the recent chronostratigraphic and isotopic data, LP-2 is assigned to the Cryogenian in the international stratigraphy (Knoll, 2000), UP-2 is early Neoproterozoic 3, and P-3 is late Neoproterozoic 3.

In the Saghro area, the studies performed on the Neoproterozoic formations show that the Cryogenian sequence (LP-2) was deposited in sedimentary basins during the pre-Pan-African extension (Lecolle et al., 1991a; Fekkak et al., 1999, 2000, 2001, 2002, 2003; Thomas et al., 2004). The early Neoproterozoic 3 sequence (UP-2) consists of volcanic and volcanoclastic rocks related to a volcanic arc (Saquaque et al., 1992). The late Neoproterozoic 3 sequence (P-3) is located along the southern flank of the Saghro massif and consists of continental molassic

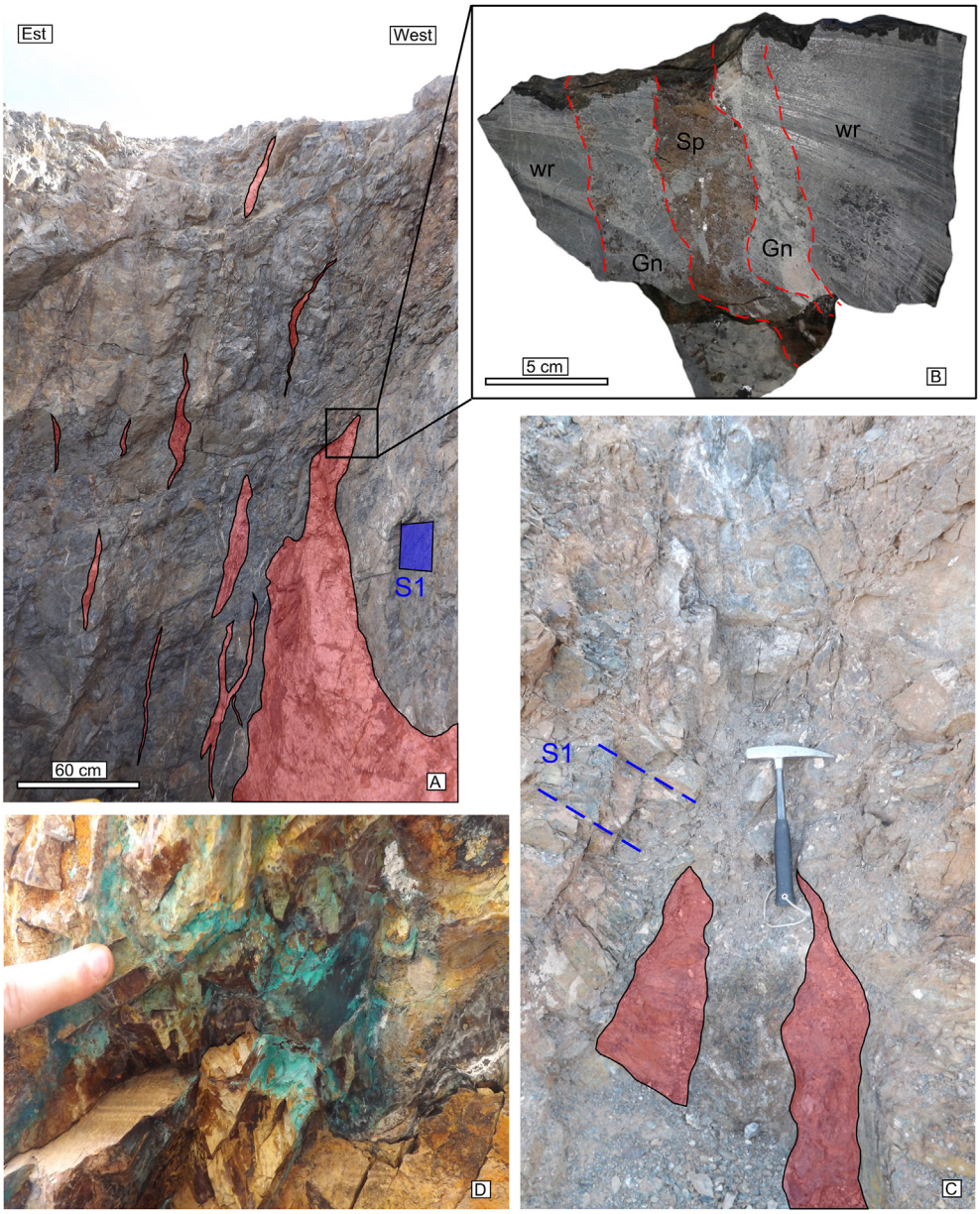

Fig. 3. (a) Sphalerite/galena bearing dyke (highlight in red) crops out in the Sidi Flah mining area. S1 indicate the main schistosity. (b) Hand sample coming from the main sphalerite/galena bearing dyke shown in Fig. 3a. The sample shows two distinct mineralizations at a distance of a few centimetres: the first located in the centre of the mineralized vein and consists mainly of sphalerite (Sp); the second one develops parallel to the previous one near the contact with the host rock (wr), and consists mainly of galena (Gn). (c) Fe, Cu-sulphides mineralization (highlight in red) crops out at NE of the Sidi Flah mining area. S1 indicate the main schistosity. (d) Surface alteration patina (mainly malachite) of Fe, Cu-sulphides mineralization. (For interpretation of the references to colour in this figure legend, the reader is referred to the web version of this article.)

deposits overlain by early Cambrian transgressive sandstone, shale and limestone. The Cryogenian sequence is exposed in the Imiter, Boumalne, Kelaat Mgouna and Sidi Flah basins as inliers within a Neoproterozoic 3 cover (Fig. 1b). These basins hosted metaturbiditic rocks and mafic to intermediate metavolcanic rocks (Fekkak et al., 2003), and their geotectonic context of deposition is a matter of debate. Both the position of the Saghro massif in front of the Bou Azzer ophiolitic suture and the occurrence of calc-alkaline volcanic rocks encouraged the authors to attribute the Cryogenian sequence to a context of a back arc basin (Saquaque et al., 1992; Ouguir et al., 1996). The analysis of metasiliciclastic rocks petrography and lava geochemistry of the Kelaat Mgouna and Boumalne Groups (Fekkak et al., 1999, 2000, 2002) shows that the detrital material was derived from a continental provenance and that the lavas of the lower and the main part of the basin filling-up have continental tholeiite and initial rift tholeiite signatures, respectively. These results led Fekkak et al. (2003) to interpret the Cryogenian sequence of Saghro as intracontinental basins that have opened during the pre-Pan-African continental breakup.

2.2. Structural setting of the Sidi Flah ore deposit

Before ERT measures, we performed a detailed geological and structural survey (Fig. 2a) of the Sidi Flah mining area, which enabled us to reconstruct the local geological setting and the stratigraphy (Fig. 2b) and to understand the relationships between mineralizations and host rocks. At least two distinct ductile deformational events connected with the Pan-African orogenesis were recognized in this area, both associated with schistosity, cleavage and folds (Fig. 2a).

The oldest macroscopic foliation in the rocks of Sidi Flah mining district represents the main foliation of the area and is associated with a pronounced deformation event (B1 phase of Pan-African deformation in Leblanc and Lancelot, 1980), characterized by schistosity developed under low-green schist facies (albite–epidote) conditions (Ezzouhairi, 1997; Lecolle et al., 1989, 1991b; Saquaque et al., 1992). The main schistosity is largely defined by chlorite, white mica, albite, quartz, opaque minerals and re-orientation of lithic grains and mono/polycrystalline grains in the siliciclastic rocks.

The original bedding of the metapelite and metasandstone is transposed and deformed by a steeply dipping schistosity (S1) which is

parallel to the axial plane of tight/isoclinals folds that generally have axis with strike from east–west to northeast–southwest, in agreement with what reported by previous authors (Saquaque et al., 1992; Benziane et al., 2008; Harrison et al., 2008; Stone et al., 2008; Walsh et al., 2008b, 2012).

Structures of a second deformation event (B2) overlap on the previous ones. This second event is connected with the collapse of the Pan-African orogenic wedge, developed in very low-green schist facies. It deformed all the previous structures (Leblanc and Lancelot, 1980; Saquaque et al., 1992) and produces a crenulation cleavage (S2), marked by recrystallization of white mica and chlorite, which is the axial plane of tight/open folds. The measured axes of these folds have a NW-SE trend in agreement with Saquaque et al. (1992) and Yazidi et al. (2008).

Finally, system of faults overlaps over the two previous ductile deformation phases (Fig. 2a). This last event may be related with the later phases of Pan-African orogenesis or to a re/activation occurred during the Paleozoic (Variscan Orogenesis), or even during the Mesozoic (Malusà et al., 2007) or Cenozoic (Harrison et al., 2008). The faults are buried by the Quaternary cover sequence and shows virtually no Pleistocenic or younger re/activation. The regional pattern of these faults system suggests predominantly left deformation consistent with left-lateral strike-slip movement under a north-northeast oriented (Fig. 1b), a horizontal maximum principal stress direction and an east-southeast oriented, horizontal least principal stress direction (Walsh et al., 2012).

The structural analysis of the Sidi Flah ore deposit has revealed the presence of two different types of sulphide bearing dykes (Fig. 3a, c). The principal ore body exploited in this mining area is a sphalerite/galena bearing dyke (Fig. 3a, b) which has a thickness between 10 cm and 1 m and about 600 m of surface extension. This dyke has been explored with direct surveys in the subsoil to a depth of about 30 m, and has a concentration in the Pb between 45% and 72%. Total Pb metal contained is estimated between 20.000 and 30.000 tonnes. Moreover, the main veins show two distinct mineralizations at a distance of a few centimetres. The first one is located in the centre of the vein and mainly consists of sphalerite. The second one develops parallel to the previous one near the contact with the host rock, and consists mainly of galena (Fig. 3b). The gangue is essentially formed by quartz, chlorite and ankerite.

A second bearing dyke marginally occupies the north-eastern sector of the mining area, and is characterized by a Fe, Cu-mixed sulphides mineralization (Fig. 3c, d). The thickness of this mineralized body is generally between 20 cm and 1 m, and its surface extension is about 400 m. The depth has never been explored. This bearing dyke was identified for the first time during the geological survey preliminary to geoelectrical study. For a more detailed petrographical and mineralogical description see §4.2.

Both mineralizations are presented as sub-vertical setting (Fig. 3a, c) with an angle generally between 70°-80° and dip direction of 250/270°. The mineralized bodies are discordant with respect to the foliation detectable on the field, and cut all the B1 and B2 structures produced by Pan-African orogenesis. Locally, some mineralized veins are set on brittle discontinuity systems, generally left strike-slip faults with north–south trend, probably generated in the last stages of collapse of the Pan-African orogenic wedge. This setting has been recently described for the Imiter mine (Cheilletz et al., 2002), the biggest Ag-Hg deposits in Morocco, located at north-east of the studied area. This ore deposit is considered to be of epithermal origin, and the silver mineralization happened during regional extension, and probable transcurrent, tectonic regime event around 550 Ma (Tuduri et al., 2005). Recent re/activation are not excluded.

3. Methods

3.1. Geoelectrical studies

As mentioned in §1, the ERT method was chosen for its relative fastness and inexpensiveness, two crucial parameters for the mining industry. Therefore, the ERT method allows to investigate large areas and distinguish easily targets with high resistivity contrast.

We developed the ERT surveys in three different phases:

1. Forward synthetic resistivity modelling and survey planning.
2. Data collection.
3. Data processing.

All these steps are fundamental to obtain reliable results useful for geological and mineralogical interpretation.

3.1.1. Forward synthetic resistivity modelling from geological target

We performed a series of synthetic resistivity models, with the aim to plan an optimal electrodic array for the specific target and to evaluate the effectiveness of ERT imaging, in a simplified scheme, similar to the site geological settings. We modelled the bearing dyke as a sub-vertical thin conductive body, dipping on the right side (to east), as the real geometry of the dyke on site. In literature, the resistivity value often refer to the sulphides as massive mineral (e.g. Pridmore and Shuey, 1976), without take into consideration effects due to the gangue and host rock. Such values can produce synthetic electrical resistivity models with underestimated resistivity values and subsequently ERT models which differ from the real conditions. Under this consideration, we followed Parasnis (1956), who conducted extensive measures of electrical resistivity on sulphides minerals with their gangue and considering the ore percentage in the samples measured. In particular, we adopted a value of 30 Ω*m as a plausible resistivity to produce reliable synthetic resistivity models.

We can resume the scheme of the bearing dyke into the host rock as follow:

- The mineralized body have a resistivity value of 30 Ω*m and variable thickness, from 0.5 m at the top, to 1.5 m at the bottom, with the sub-vertical setting;
- The host rock with resistivity value of 1000 Ω*m.

The starting synthetic resistivity model has been discretized in a regular mesh trough Res2Dmod-Geotomo software (forward modelling). The correspondent ERT models were carried out using Res2Dinv with the robust constrain (Loke, 2012) and same parameters applied for the real data, as explained in the § 3.1.3.

The acquisition array, both for synthetic resistivity models and for field surveys, was made by 96 electrodes with interelectrodic steps of 2 and 3 m and quadripolar configuration Dipole-Dipole (DD), Wenner-Schlumberger (WS) and, only for field surveys, Schlumberger Reciprocal (SR).

The first was taken into consideration for its high sensitivity for lateral resistivity variations, the second for its moderate sensitivity in both vertical and horizontal direction and high signal/noise ratio (Loke, 2012), and the last, with similar characteristic to the WS, for the high productivity due to the simultaneous acquisition of several quadripoles (up to 9). We used WS configuration with the aim to compare and validate the results of Schlumberger Reciprocal quadripol, more productive in terms of ERT models in the same time. Furthermore, the DD configuration has the lowest signal strength and a lower sensitivity to the vertical changes in resistivity regarding to the SR and WS configuration.

We tried four different models on the basis of the geological target:

- 1 sub-vertical body into the host rock, with electrodic steps of 2 and

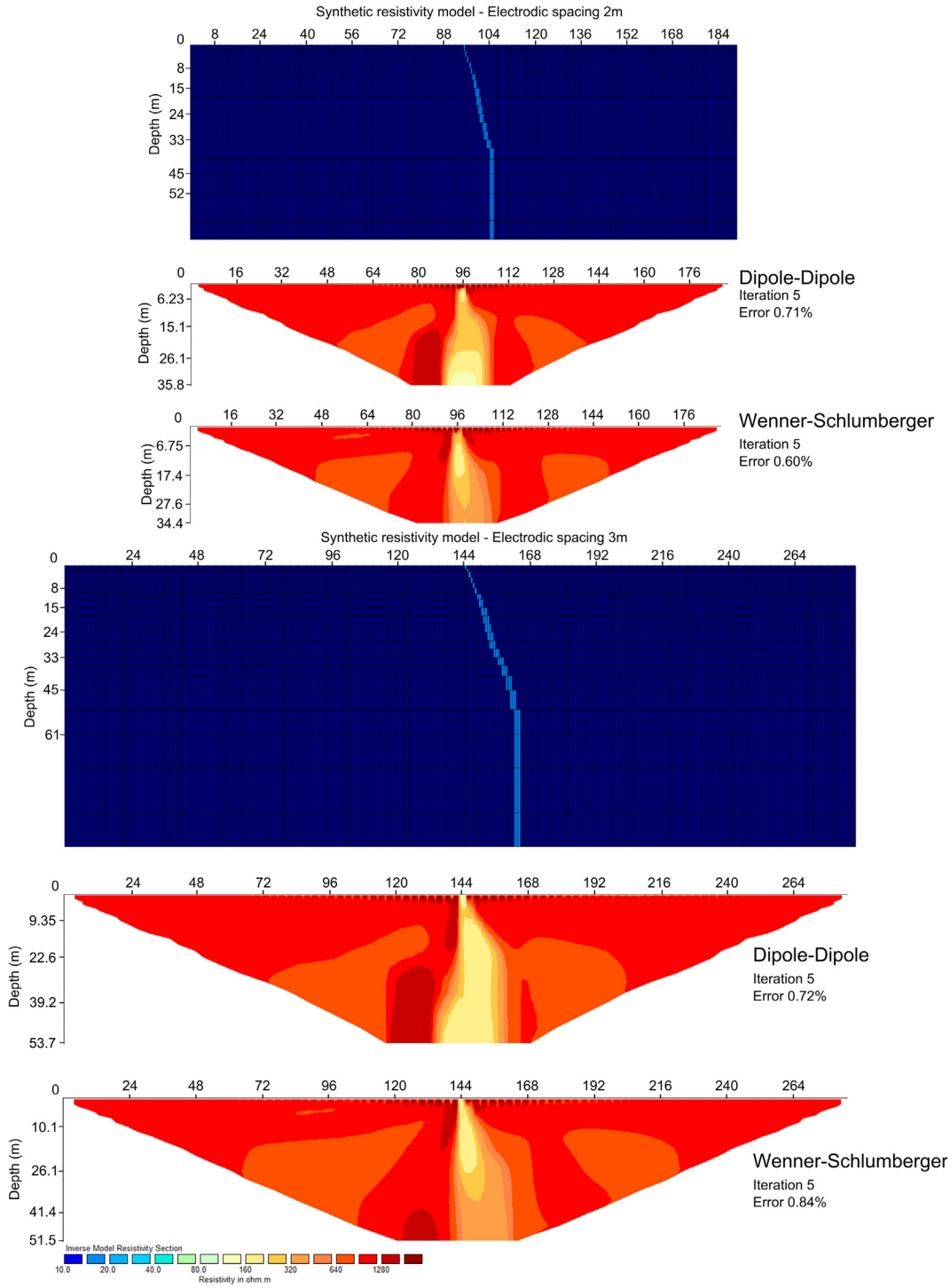

Fig. 4. Example of synthetic resistivity models of theoretical terrain developed in order to plan the survey electrodic step and to evaluate the resistivity response differences, between Dipole-Dipole and Wenner-Schlumberger quadripolar configuration with starting models similar to the real target.

3 m and DD configuration (Fig. 4);

- 1 sub-vertical body into the host rock, with electrodic steps of 2 and 3 m and WS configuration (Fig. 4).

3.1.1.1. Synthetic resistivity modelling to evaluate different ERT response for sub-vertical conductive body. The starting model is a sub-vertical conductive body of thickness variable from 0.5 m, at the top, to 1.5 m, at the bottom, with a resistivity value of 30 Ω*m, into a volume with resistivity value of 1000 Ω*m (Fig. 4). Greater is the electrodic step, deeper is the ERT imagine but on the other hand the spatial resolution tends to decrease increasing the depth of survey.

In the WS configuration, the resistivity values of the conductive body also tend to increase with the depth, conversely the DD configuration gives resistivity values lower at the bottom of the ERT models (Fig. 4). The DD produced sharper vertical border than WS, probably due to the higher sensitivity to the lateral variation, as well known in literature (e.g. Loke, 2012; Okpoli, 2013; Moreira et al., 2016). On the other hand, the WS led to conductive shapes more similar to the initial model in terms of geometry than DD, which from the middle part of the ERT model, tends to expand the conductive body on the left side.

3.1.2. Data collection

In order to carry out high-resolution geoelectrical resistivity measures in the Sidi Flah mining area, we used Syscal-Pro Switch of IRIS Instruments (IIRIS Instruments, 2003). This instrumentation is intended for intensive explorations of the underground, using the direct current method. It allows to carry out the resistivity measurements completely in automatic way and record the variations of resistivity with the depth (vertical electrical survey) and with the lateral extension of the profile (electrical profile). Furthermore, it can measure the electrical chargeability of subsurface materials (Induced Polarization).

The instrument is composed of a single case containing:

- An internal switch that allows the employment of 96 electrodes.
- A georesistivimeter formed by a transmitter and a receiver.

The instrument allows automatically to perform the measures based on the voltage values, stacking number and Q factor set up by the operator. The maximum output values are 800 V in the switch mode and 1000 V in the manual mode, 2.5 A and 250 W with the internal transformer and battery 12 V, which can be increased up to 1200 W with an external generator and AC/DC (IRIS Instruments, 2003).

The system of acquisition (up to 10 channels) allows to carry out a maximum of 10 readings at the same time, remarkably reducing the time of acquisition. The time of injection/measurement is variable between 0.25 s and 8 s. The maximum configuration is 96 metallic electrodes with galvanic connection subdivided in 4 multi-conductor cables.

We performed a series of synthetic resistivity models in order to verify the ERT response and to choose the electrodical step for carrying out useful surveys, as seen at §3.1.1

In connection with the site logistics and the geological survey target, we distributed 15 ERT lines across the study area, whose location is shown in Fig. 2a. Later, knowing the main structural directions of the mixed sulphides bearing dykes, we planned orthogonal acquisition lines to obtain the real aspect of the ore bodies.

In order to explore the subsurface and highlight the lithological variations both vertical and horizontal, we acquired over the first profile (*tomo_5_bis*) three datasets with Dipole-Dipole (DD) (Fig. 5a), Schlumberger Reciprocal (SR) (Fig. 5b) and Wenner-Schlumberger (WS) (Fig. 5c) quadripolar configurations. After compared the SR and WS in a preliminary analysis as explained in §4.1, we have chosen to acquire remaining lines using the DD and SR configurations.

As demonstrated in the synthetic resistivity models described in §3.1, we have chosen 2 and 3 m as electrodic step with 96 electrodes, with the aim to acquire high resolution data. As parameters for quality control in acquisition we have chosen minimum stack 3, maximum stack 6 with Q factor threshold equal to 5% and 400 V as potential difference for the injection dipole.

3.1.3. Data processing

Data processing can be divided in 2 steps. In the first step were removed bad data using threshold values represented by measurements of st-dev > 5%, abs (ΔV) < 1 mV, apparent resistivity < 0 Ω*m and resistivity values that appears as outliers. In the second step we carried out the tomographic inversion starting from apparent resistivity values trough Res2Dinv software V. 4.03.13. An inversion routine used by the program is based on the smoothness-constrained least-squares method (De Groot-Hedlin and Constable, 1990; Sasaky, 1992). However, to process data acquired over a high conductive body within high resistivity host rocks, we applied the Robust constrain, more consistent with the site geological setting. This inversion method gives significantly better results in presence of sharp boundaries instead of smoothness-constrained least-squares method (Loke, 2012). The purpose of this software is to determine the resistivity of rectangular blocks composing an apparent resistivity pseudo-section, which agrees with the field measurements. The optimization step reduces the difference between the calculated and measured apparent resistivity values by adjusting the resistivity of the model blocks.

The iterations stop when reach a defined number of iterations or the variation in terms of RMS, between two subsequent iterations, is lower than a threshold value; on other hand additional iterations do not give substantial improvement at the results.

The 2D model used by this program divides the subsurface into a number of rectangular blocks respect to the electrodic step. For all the inversions, we utilized the model refinement tool with the aim to enhance the model discretization and take into consideration large horizontal resistivity variations of the ground. Moreover, due to the prevalent sub-vertical disposition of conductive bodies, we used as "*Vertical to horizontal flatness filter ratio*" the value of 1.5 and severe reduction effect of side blocks. At last, we applied "*Edit data - RMS statistic error*" to remove noisy data, where the percentage difference between the observed and calculated apparent resistivity values was far and well separated from the average values.

3.2. Petrographic and mineralogic studies

Several centimetre samples were collected for mineralogic and petrographic characterization. Samples were collected both from the area interested by the sphalerite/galena mineralization, and from the area with the Fe, Cu-sulphides mineralization.

X-ray powder diffraction (XRPD) was performed by a Philips X'Pert PRO PW 3040/60 with X'Celerator PW 3015 detector. Millimetric to centimetric rock fragments were extracted from significant areas of wall rocks, mineralized veins and alteration areas.

Thin sections, perpendicular to the mineralized veins or cutting the alteration areas, were observed by polarized light Optical Microscopy (OM) and Scanning Electron Microscopy (SEM). SEM was performed using a Philips XL30, operating at 20 kV and equipped with an EDAX-DX4 energy dispersive spectrometer (EDS), providing chemical analysis for atoms heavier than C. Both backscatter electrons (BSE) and secondary electrons (SE) were used for imaging.

4. Results

4.1. ERT

In order to evaluate differences in terms of resistivity response and data quality, we compared the DD, SR and WS quadripolar configurations over the same line (*tomo_5_bis*) (Fig. 5). One of the main differences showed from the data is the Q factor of quadripoles acquired, generally higher for the DD compared to the SR and WS electrodic configurations (Fig. 6). The SR registered slightly different results in term of Q factor of quadripoles measurements regarding to WS acquisitions (Fig. 6), and also in terms of ERT models there were minimal differences (Fig. 5). A common check consists in the individuation of the model at the iteration after which the RMS error change is insignificant in results improvement (Loke, 2012). The RMS curves for the all processed data did not show substantial variations from the third to the fifth iteration for the SR and DD resistivity models, with the last quadripolar configuration showing on average much higher RMS values (Fig. 7). The RMS used to validate the model has chosen lower than 3.5 for SR method; differently the DD showed a variety of final values which ranging from about 4.3 to 27.6 and their variation are not appreciable between the two last iterations. In this case we opted to use, as ERT models, the last iteration. In Table 1 a complete description of acquired quadripoles, processed quadripoles, iterations and related RMS values are reported.

In particular, comparing the DD, SR and WS ERT models of the line *tomo_05_bis* (Fig. 5), we can see a substantial similarity between the three configurations until the progressive of 160 m, with a medium-conductive body centred at the progressive of 96 m. The DD configuration, from the progressive of 160 m to the end of ERT model, shows

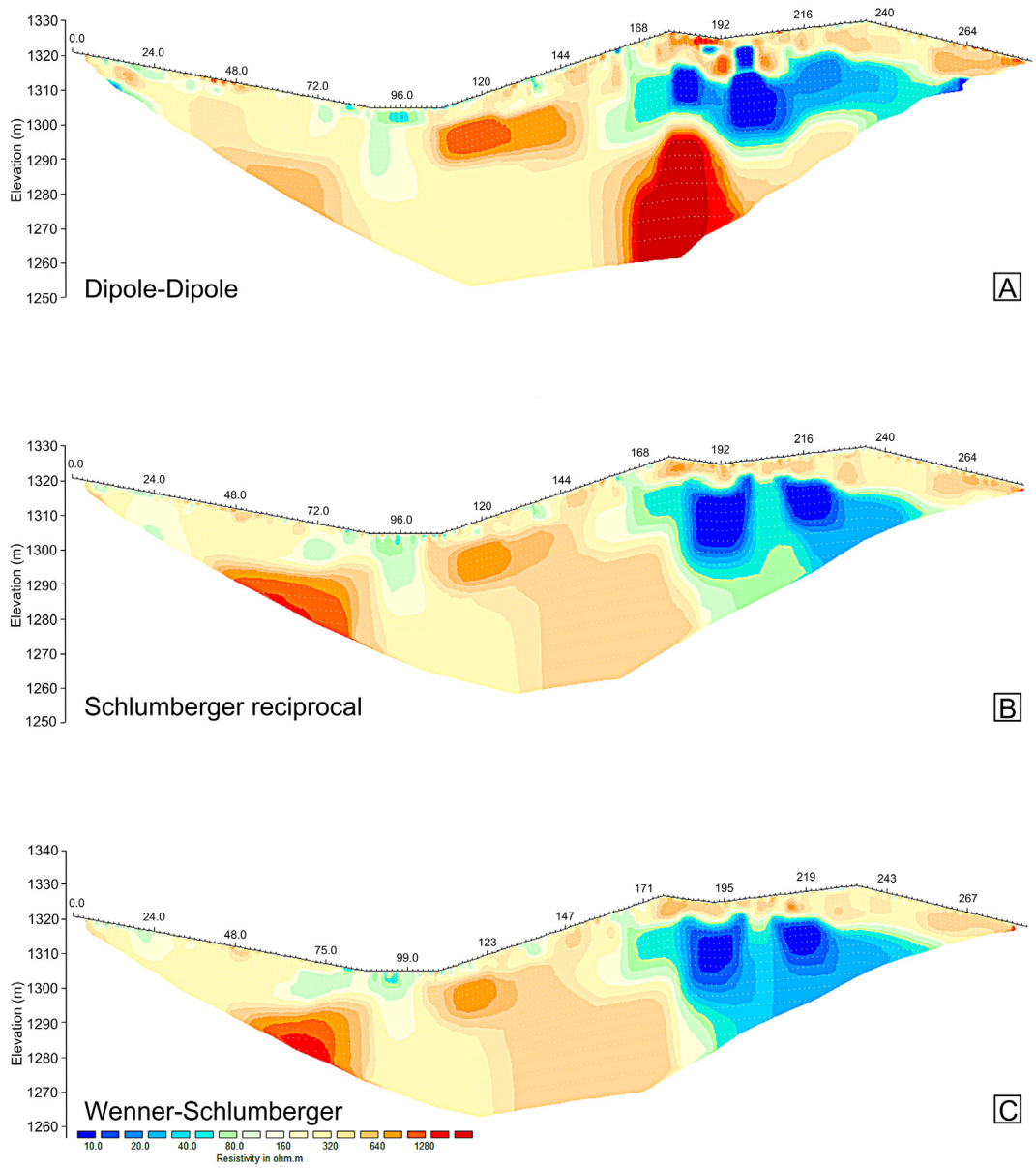

Fig. 5. Comparison among the three configuration on the line *tomo_05_bis*. (a) ERT model acquired with DD configuration. (b) ERT model acquired with SR configuration. (c) ERT model acquired with WS configuration. SR and WS provide approximately the same results while DD gives results slightly different for the right part of the tomography, showing a sharp vertical increasing of resistivity below the conductive body.

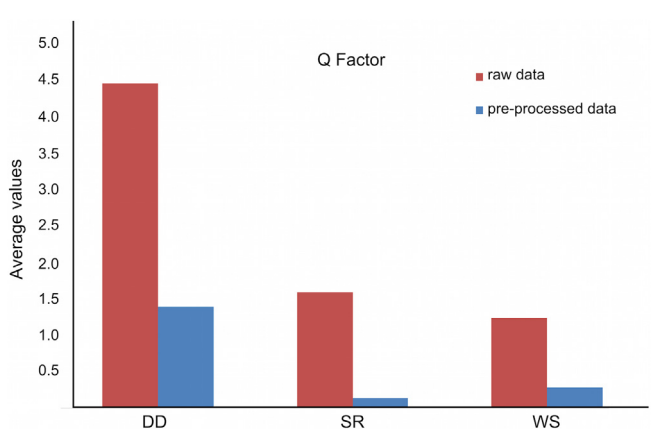

Fig. 6. Comparison between Q factor for raw and filtered data for the line *tomo_5_bis*; for raw data we consider all quadripoles measured without rejected values due to Q > 5% and resistivity < 0 Ω*m.

approximately a unique sub-horizontal conductive body with sharp vertical variations, above a very high resistivity body. In agreement with DD, the SR and WS show a vertical variation at the depth of about 6 m, from resistive to conductive values. Partially in contrast with DD configuration, the SR and WS show two distinct conductive bodies without the vertical increasing of resistivity at the bottom.

The SR and WS revealed similar quality in acquired data (Fig. 6) and the results in terms of resistivity models for the aim of this work, can be considered equivalent; this fact led us to acquire remaining lines with the SR. In general, as auspicated the DD (Figs. 8–10) and SR (Figs. 11–13) provided similar results in terms of main conductive anomalies, nevertheless the DD showed extreme resistivity variations and in few cases chaotic results compared to the SR resistivity models.

With the aim to compare electrical resistivity images from the two quadripolar configurations acquired, both DD (Figs. 8–10) and SR results (Figs. 11–13) are shown. However, we interpreted only the SR as further explained in §5.

All ERTs performed in the studied area can be grouped in 3 distinct

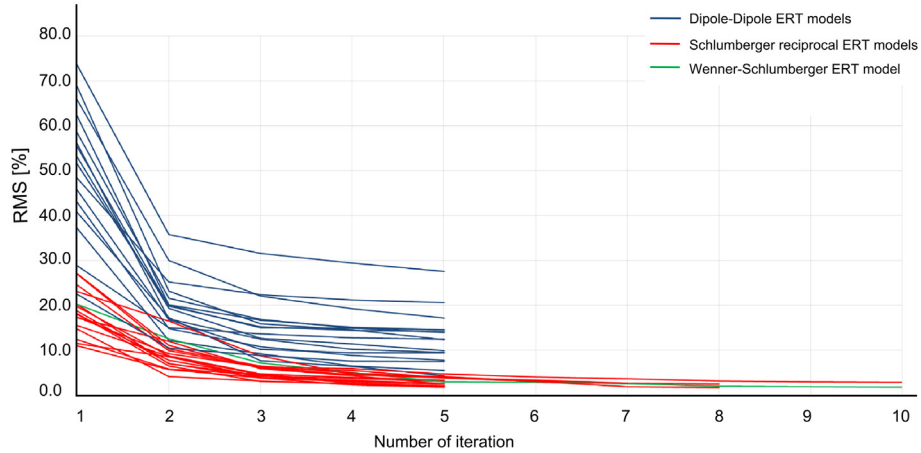

Fig. 7. RMS chart for DD inverted model (in blue), SR inverted model (in red) and WS inverted model (in green). RMS curves show the high variability for DD configuration. (For interpretation of the references to colour in this figure legend, the reader is referred to the web version of this article.)

Table 1
Parameters of the ERT models, carried out in the Sidi Flah mining area, divided in DD, SR and WS configuration. For each line, the acquired and processed quadripoles, number of iteration chosen for the ERT model and corresponding RMS value are reported.

id_profile	Quadripolar configuration	Acquired data	Processed data	Iteration	RMS
tomo_01	DD	4409	3842	5	20.6
	SR	3789	3616	5	3
tomo_01_bis	DD	4409	3567	5	12.5
	SR	3789	3574	4	3
tomo_02	DD	4409	3782	5	5.5
	SR	3789	3737	4	3.1
tomo_03	DD	4409	4114	5	9.5
	SR	3789	3750	5	2.5
tomo_04_bis	DD	4409	3596	5	14.6
	SR	3789	3572	5	3.3
tomo_04	DD	4409	3421	5	14.1
	SR	3789	3588	4	3.4
tomo_05	DD	4409	4144	5	4.3
	SR	3789	3753	3	3.1
tomo_05_bis	DD	4409	3353	5	17.2
	SR	3789	3499	6	3.1
	WS	2210	2073	5	3
tomo_06	DD	4409	3939	5	7.8
	SR	3789	3749	4	3
tomo_07	DD	4409	3639	5	9.4
	SR	3789	3523	3	3.1
tomo_08	DD	4409	3891	5	12.3
	SR	3789	3607	6	3
tomo_08_bis	DD	4409	3362	5	13.9
	SR	3789	3502	6	3.4
tomo_09_bis	DD	4409	3486	5	10
	SR	3789	3605	6	3.1
tomo_09	DD	4409	3435	5	27.6
	SR	3789	3451	8	3.2
tomo_10	DD	4409	4079	5	7.5
	SR	3789	3606	3	2.3

geographical areas, defined respectively as "Area 1", "Area 2" and "Area 3", from south to north (Figs. 11–13) on the base of their different resistivity response. Resistivity values revealed by ERT in the study area range from lower than 10 Ω*m up to 2000 Ω*m.

It is possible to recognize a sub-vertical conductive body, approximately at the centre of the ERT models, with resistivity values lower than 150 Ω*m, and marked with dashed lines as zone "A" (Figs. 11–13). This conductive body shows continuity through the all ERT models, from "Area 1" to "Area 3", with strong tendency of resistivity reduction in the northern part of the studied area, where the minimum values of electrical resistivity were registered (Figs. 11–13). In "Area 1", the lines *tomo_4* and *tomo_4_bis* denoted the absence of the vertical body described as zone "A".

In addition in "Area 2" and "Area3", on the right side of the resistivity models, appears another conductive body (zone "B"), with resistivity values lower than the body located in the centre of ERT models (zone "A"). Starting from the right part of the lines *tomo_5_bis* to the *tomo_9_bis*, we can distinguish a large zone with resistivity values lower than 80 Ω*m (zone "B") (Figs. 12 and 13). Moreover, from the top of this portion to the ground surface a zone with resistivity values higher than 300 Ω*m is always present (zone "D"; Figs. 12 and 13).

In "Area 1" and "Area 2" we can distinguish a sub-horizontal conductive layer (zone "C") which extends from the ground surface up to a maximum deep of 10 m and characterized by resistivity values lower than 100 Ω*m. This layer generally is located into the valley line (Figs. 11 and 12).

4.2. Petrography and mineralogy

4.2.1. Wall rocks

The Sidi Flah mixed sulphides are hosted within the Precambrian basement of the Saghro massif well described by Fekkak et al. (2003). Specifically, the ore bodies occur principally within metasandstone and phyllite of Aït Witfao Fm, granitic dykes, and in rare cases in metalimestone and metachert.

The metasandstone of Aït Witfao Fm (Fig. 14a) is mainly formed by quartz and feldspar, lithic fragments and accessory minerals (epidote and zircon). Polycrystalline quartz grains are less abundant than monocrystalline ones, and the amount of K-feldspar and plagioclase is variable. The average composition of the metasandstone is from greywacke to feldspathic-greywacke in according to Fekkak et al. (2003). In the finer grain size portions, the main schistosity (S1) is well evident and it is marked by recrystallization of phyllosilicates.

The phyllite of Aït Witfao Fm (Fig. 14b) is made by an alternation of lepidoblastic layers of white mica and chlorite, and granoblastic layers of quartz, albite, opaque minerals and rare epidote and zircon. This alternation of lepidoblastic and granoblastic levels mark the main schistosity (S1).

In the Aït Witfao Fm, different stacks of lava flows are present, preserving in some cases the pillow-lava structures (Fig. 14c), indicating underwater extrusion coeval with the siliciclastic sedimentation. The rocks are relatively fresh in the massive inner part of pillows, where relict of microlitic texture is preserved with plagioclase laths (An_{10-49}), micro-crystals of magnesio-hornblende, secondary epidote, calcite and opaque minerals. Chemical compositions correspond to fairly evolved basalts.

Ten to fifty meters elongated and oval-shaped bodies of carbonate

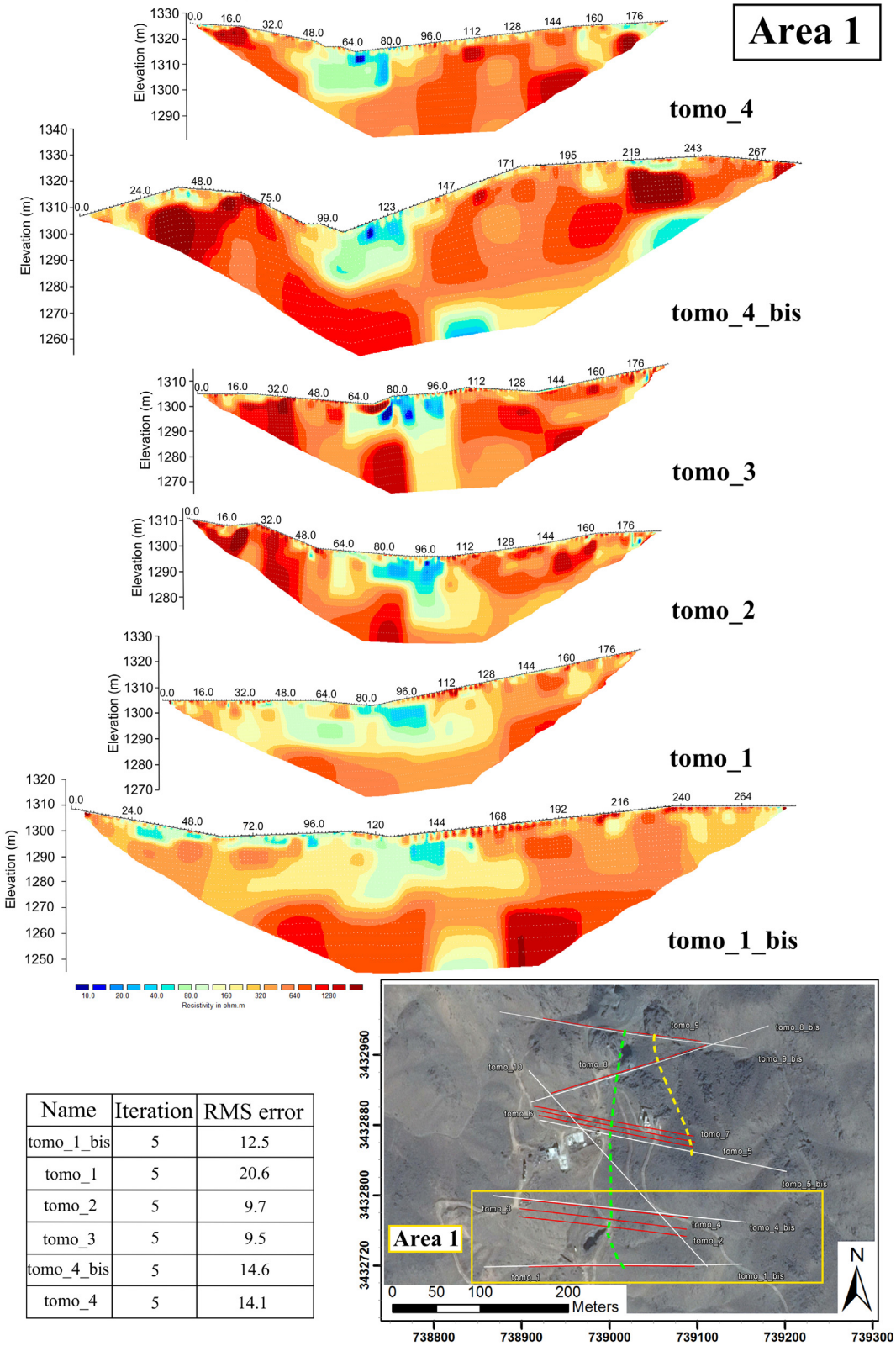

Name	Iteration	RMS error
tomo_1_bis	5	12.5
tomo_1	5	20.6
tomo_2	5	9.7
tomo_3	5	9.5
tomo_4_bis	5	14.6
tomo_4	5	14.1

Fig. 8. DD ERT models of "Area 1". In the table at the bottom left the number of iterations and RMS of each single ERT model are reported. At the bottom right the location of the 2D geoelectrical lines acquired in the mining area is reported.

and siliceous rocks, including metalimestone (Fig. 14d) and metachert or jasper (Fig. 14e), are interbedded throughout the series, conformably with the stratification (Fig. 2b). They are more abundant just below and above the basaltic lava flows.

The metasedimentary rocks are intruded by Ediacaran granites (Fig. 14f), and generally these intrusive rocks occur both in stock-like plutonic bodies and dikes (Fig. 2a, b). They have largely peraluminous to slightly metaluminous, high-K calc-alkaline compositions

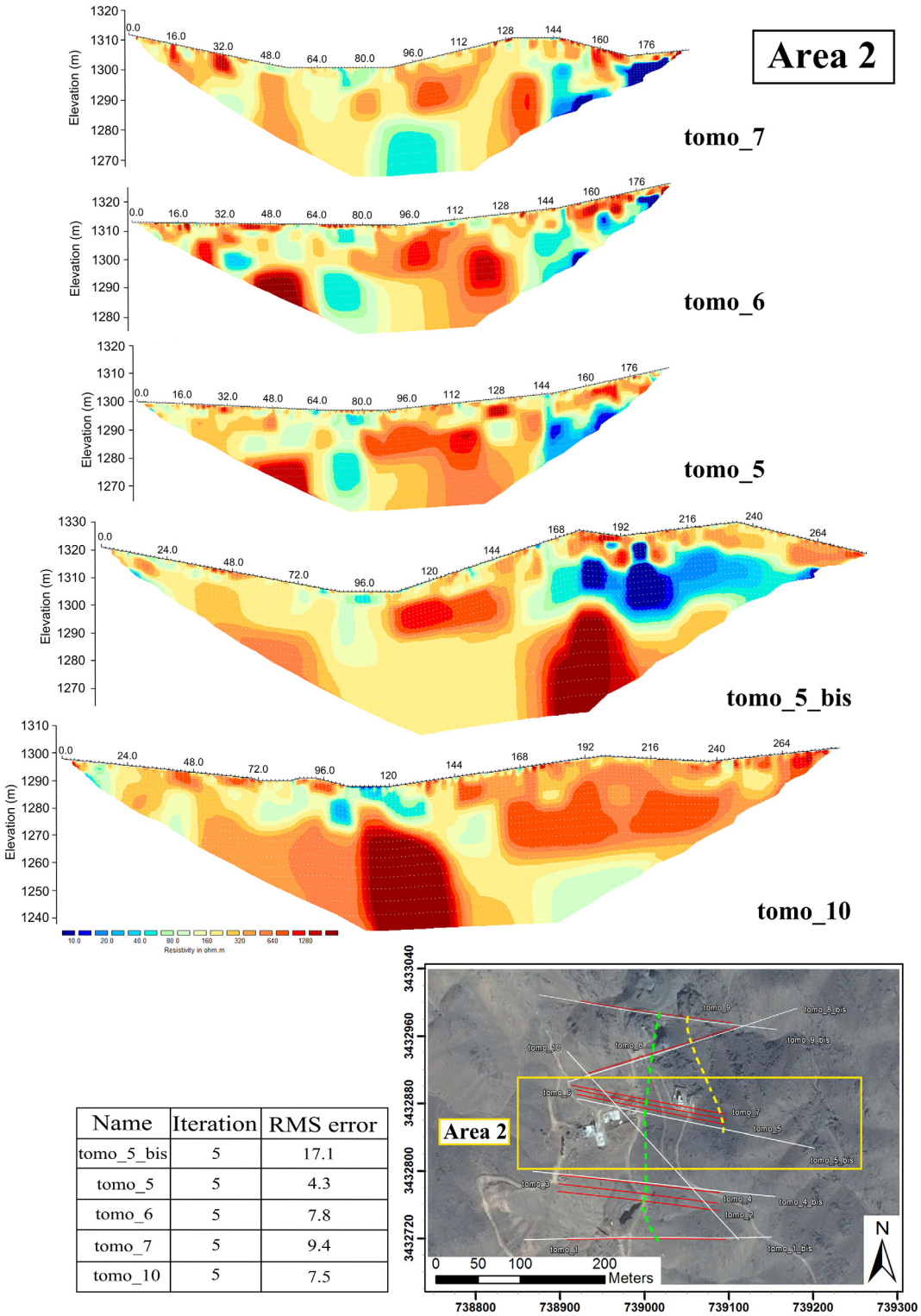

Name	Iteration	RMS error
tomo_5_bis	5	17.1
tomo_5	5	4.3
tomo_6	5	7.8
tomo_7	5	9.4
tomo_10	5	7.5

Fig. 9. DD ERT models of "Area 2". In the table at the bottom left the number of iterations and RMS of each single ERT model are reported. At the bottom right the location of the 2D geoelectrical lines acquired in the mining area is reported.

(Hindermeyer et al., 1977; Saadane, 2004; Gasquet et al., 2005, 2008; Massironi et al., 2008; Walsh et al., 2012). These intrusive rocks are principally muscovite-biotite granite, and consist of plagioclase, occurring as large sausseritized euhedral crystals with albitic rims, quartz and muscovite and biotite. Alkali feldspar is fractured and alterated to sericite and kaolinite. Chlorite and epidote (sausserite) are low-grade alteration products of biotite and plagioclase. Accessory minerals are zircon, apatite and opaque minerals. These rocks are dated by the SHRIMP-RG U-Pb zircon method to 570 ± 5 Ma (Walsh et al., 2012), and probably represent an apophysis of Bouskour granite which extensively outcrop at east and southeast of the studied area.

4.2.2. Sphalerite/galena mineralization

Samples consist of metapelitic wall rocks cut by quartz or quartz-

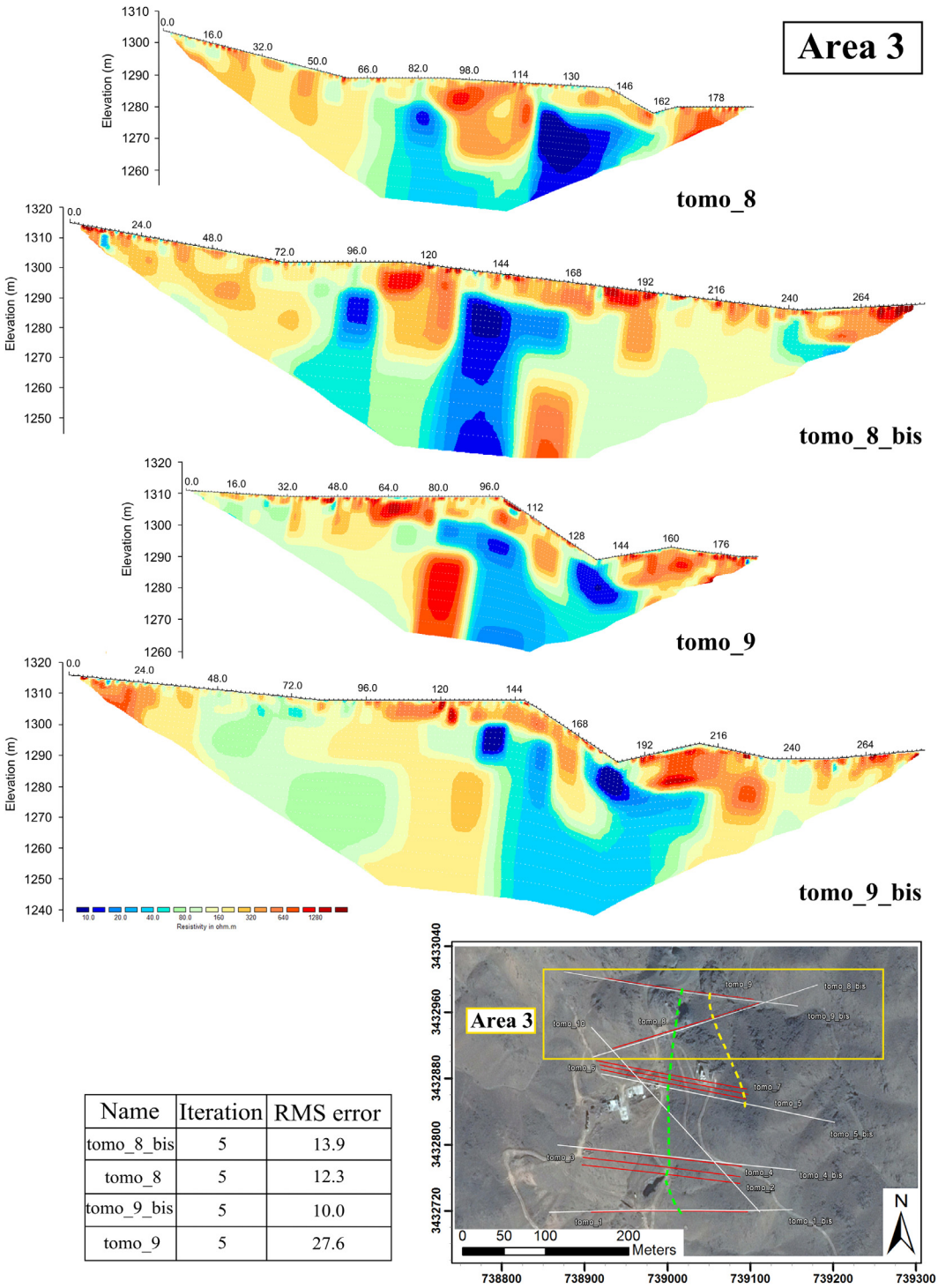

Name	Iteration	RMS error
tomo_8_bis	5	13.9
tomo_8	5	12.3
tomo_9_bis	5	10.0
tomo_9	5	27.6

Fig. 10. DD ERT models of "Area 3". In the table at the bottom left the number of iterations and RMS of each single ERT model are reported. At the bottom right the location of the 2D geoelectrical lines acquired in the mining area is reported.

carbonate mineralized veins (Fig. 15a). The wall rock is mainly made of quartz, albite and chlorite, with K-feldspar, iron oxides and apatite as accessory minerals. Mineralized veins may have thickness up to 5 cm and are filled by preeminent millimetric quartz crystals and local chlorite and carbonate domains (calcite, dolomite and micrometric ankerite crystals) (Fig. 15b). The central portion of the vein is normally occupied by sphalerite, while the rim is occupied by galena (Fig. 3b and 15c). Fragments of wall rocks are also common inside the veins.

Sphalerite has a significant iron content, with average formula $Zn_{0.92}Fe_{0.08}S$. Sphalerite crystals also host micrometric galena crystals and are locally altered in reddish masses of hemimorphite $Zn_4Si_2O_7(OH)_2{\cdot}H_2O$ (Fig. 15d).

Galena crystals have a homogeneous composition and no EDS signal from different metals than Pb was ever observed. Galena is always associated with carbonate domains and occasional pyrite micro-crystals. Galena is locally surrounded by two halos of alteration, the inner one made of anglesite $PbSO_4$, and the outer one of cerussite $PbCO_3$ (Fig. 15e).

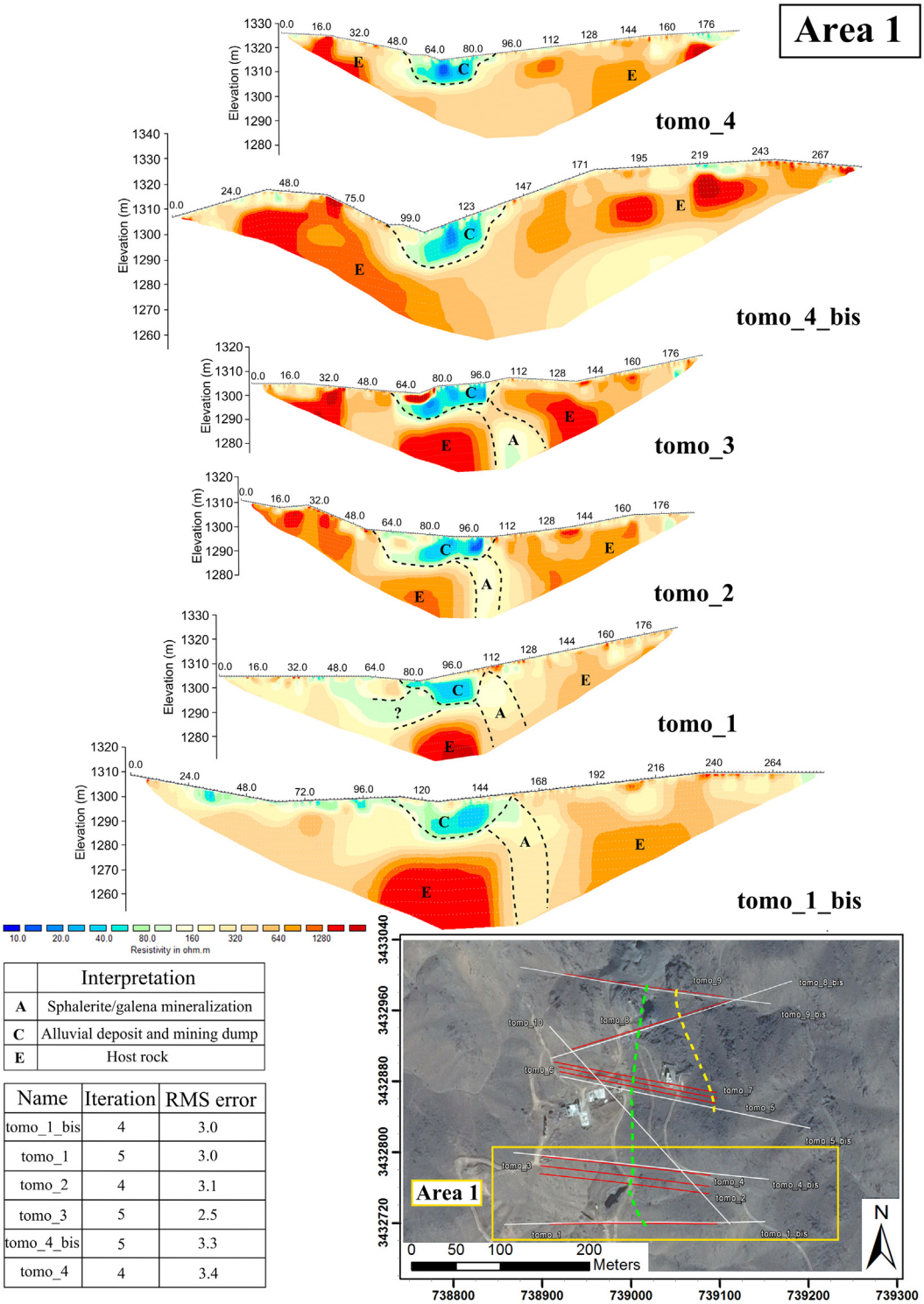

	Interpretation
A	Sphalerite/galena mineralization
C	Alluvial deposit and mining dump
E	Host rock

Name	Iteration	RMS error
tomo_1_bis	4	3.0
tomo_1	5	3.0
tomo_2	4	3.1
tomo_3	5	2.5
tomo_4_bis	5	3.3
tomo_4	4	3.4

Fig. 11. SR ERT models of "Area 1". In the table at the bottom left the number of iterations and RMS of each single ERT model are reported. At the bottom right the location of the 2D geoelectrical lines acquired in the mining area is reported. The green and the yellow dotted lines represent respectively the envelope of the sphalerite/galena bearing dyke (zone "A") and the Fe, Cu-sulphide mineralization (zone "B"), as inferred by ERT models and surface data. Zone "C" and "E" are respectively representative of alluvial deposits and mining dump and host rocks. (For interpretation of the references to colour in this figure legend, the reader is referred to the web version of this article.)

4.2.3. Fe, Cu-sulphides mineralization

Samples mainly consist of quartz, with occasionally enclosed metapelitic fragments (Fig. 15f). The fact that quartz is the main component suggest that mineralized veins were originally thicker that the typical hand sample size, i.e. more than 20 cm.

Rare very altered chalcopyrite $CuFeS_2$ domains can be detected enclosed in the quartz matrix (Fig. 15g). Conversely, dark, greenish, bluish or brown-reddish haloes of alteration minerals are ubiquitously present, hosted in specific domains or geodes, or intercalated in-between quartz grain boundaries. Typical cryptocrystalline alteration minerals are chalcocite Cu_2S, chrysocolla $Cu_2H_2Si_2O_5(OH)_4{\cdot}n(H_2O)$, malachite $Cu_2CO_3(OH)_2$ and different sulphates, arsenates, carbonates

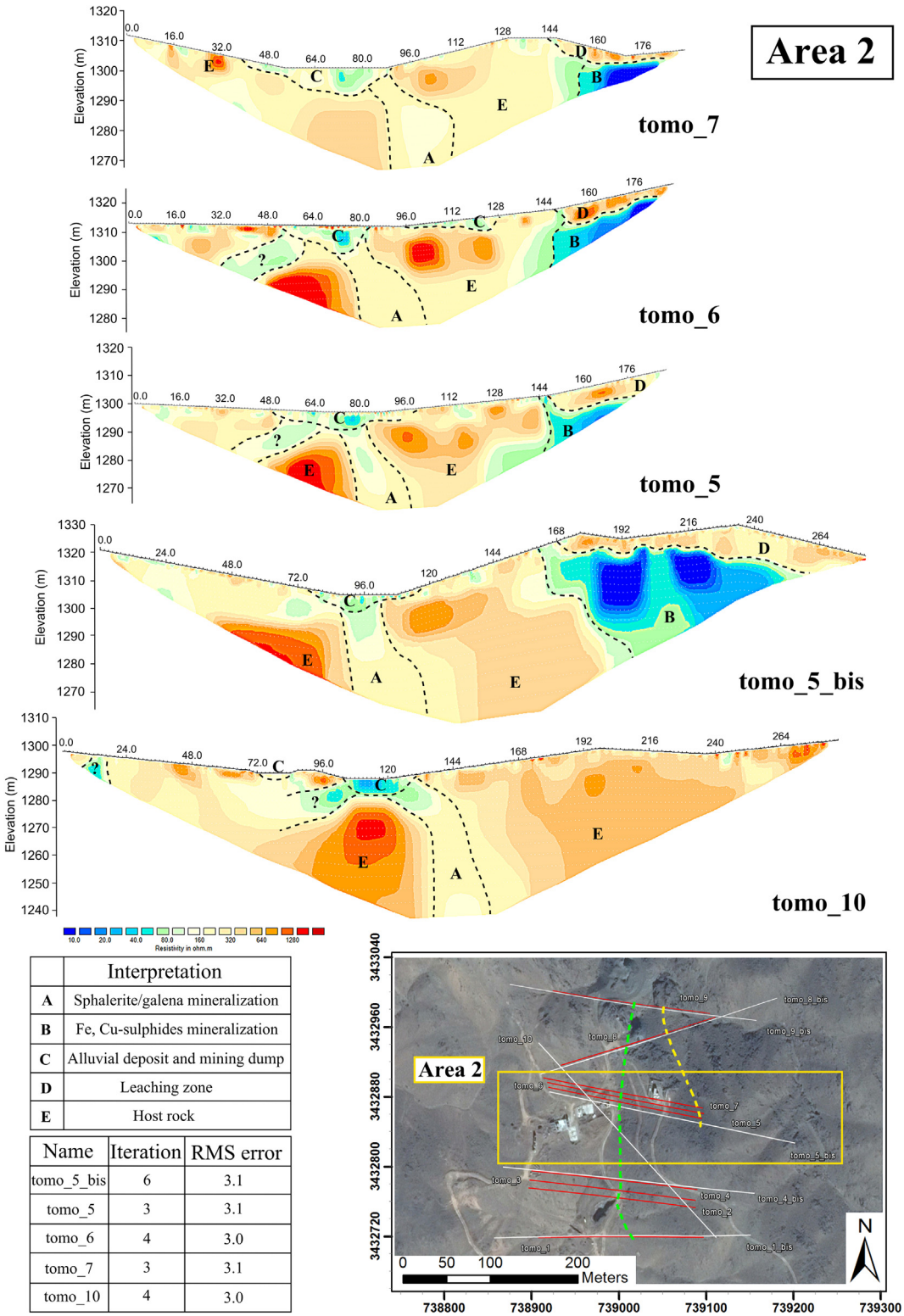

	Interpretation
A	Sphalerite/galena mineralization
B	Fe, Cu-sulphides mineralization
C	Alluvial deposit and mining dump
D	Leaching zone
E	Host rock

Name	Iteration	RMS error
tomo_5_bis	6	3.1
tomo_5	3	3.1
tomo_6	4	3.0
tomo_7	3	3.1
tomo_10	4	3.0

Fig. 12. SR ERT models of "Area 2". In the table at the bottom left the number of iterations and RMS of each single ERT model are reported. At the bottom right the location of the 2D geoelectrical lines acquired in the mining area is reported. The green and the yellow dotted lines represent respectively the envelope of the sphalerite/galena bearing dyke (zone "A") and the Fe, Cu-sulphide mineralization (zone "B"), as inferred by ERT models and surface data. Zone "C", "D" and "E" are respectively representative of alluvial deposits and mining dump, leaching zone, and host rocks. (For interpretation of the references to colour in this figure legend, the reader is referred to the web version of this article.)

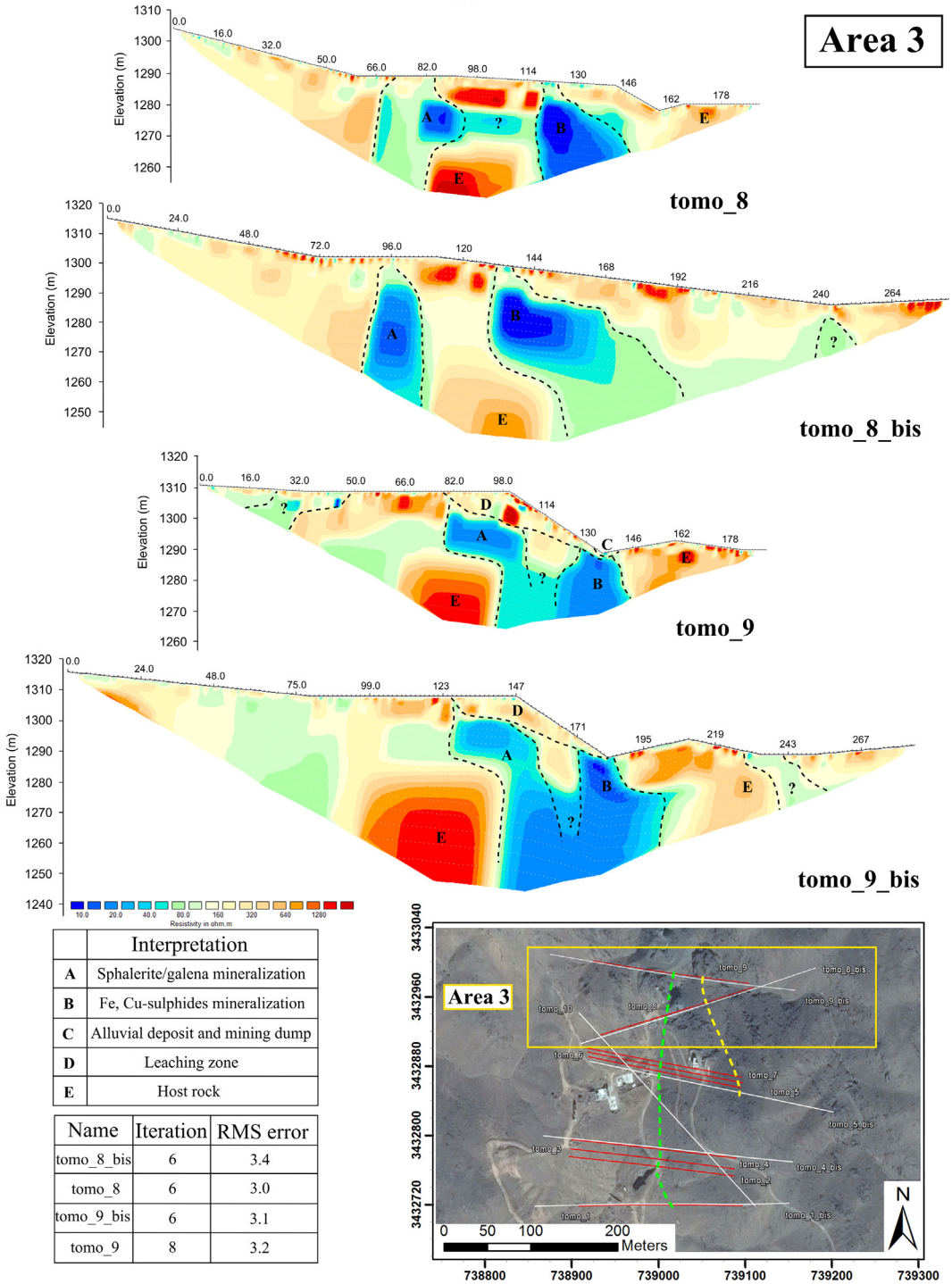

	Interpretation
A	Sphalerite/galena mineralization
B	Fe, Cu-sulphides mineralization
C	Alluvial deposit and mining dump
D	Leaching zone
E	Host rock

Name	Iteration	RMS error
tomo_8_bis	6	3.4
tomo_8	6	3.0
tomo_9_bis	6	3.1
tomo_9	8	3.2

Fig. 13. SR ERT models of "Area 3". In the table at the bottom left the number of iterations and RMS of each single ERT model are reported. At the bottom right the location of the 2D geoelectrical lines acquired in the mining area is reported. The green and the yellow dotted lines represent respectively the envelope of the sphalerite/galena bearing dyke (zone "A") and the Fe, Cu-sulphide mineralization (zone "B"), as inferred by ERT models and surface data. Zone "C", "D" and "E" are respectively representative of alluvial deposits and mining dump, leaching zone, and host rocks. (For interpretation of the references to colour in this figure legend, the reader is referred to the web version of this article.)

and hydroxides of Cu, Fe, Sb, Ni, Mn, Ca, Co and Mg (Fig. 15h). Millimetric dark-blue crystals of azurite $Cu_3(CO_3)_2(OH)_2$ can be also found inside geodes (Fig. 15i).

5. Discussion

Rock resistivity is a complex parameter depending from: i) differences in chemical properties of the pore water; ii) structure of pore volume; iii) type and amount of minerals; iv) grain sizes (Nelson and Van Voorhis, 1983; Kemna et al., 2000; Kneisel, 2006). In this perspective, the resistivity variation could be produced by several characteristics of the subsoil, and its interpretation is not so easy without other constrains.

Previous studies carried out on mixed sulphide ore bodies (e.g Tavakoli et al., 2012, 2016) have shown that it is possible to discriminate, with the ERT method, the mineralized body, characterized

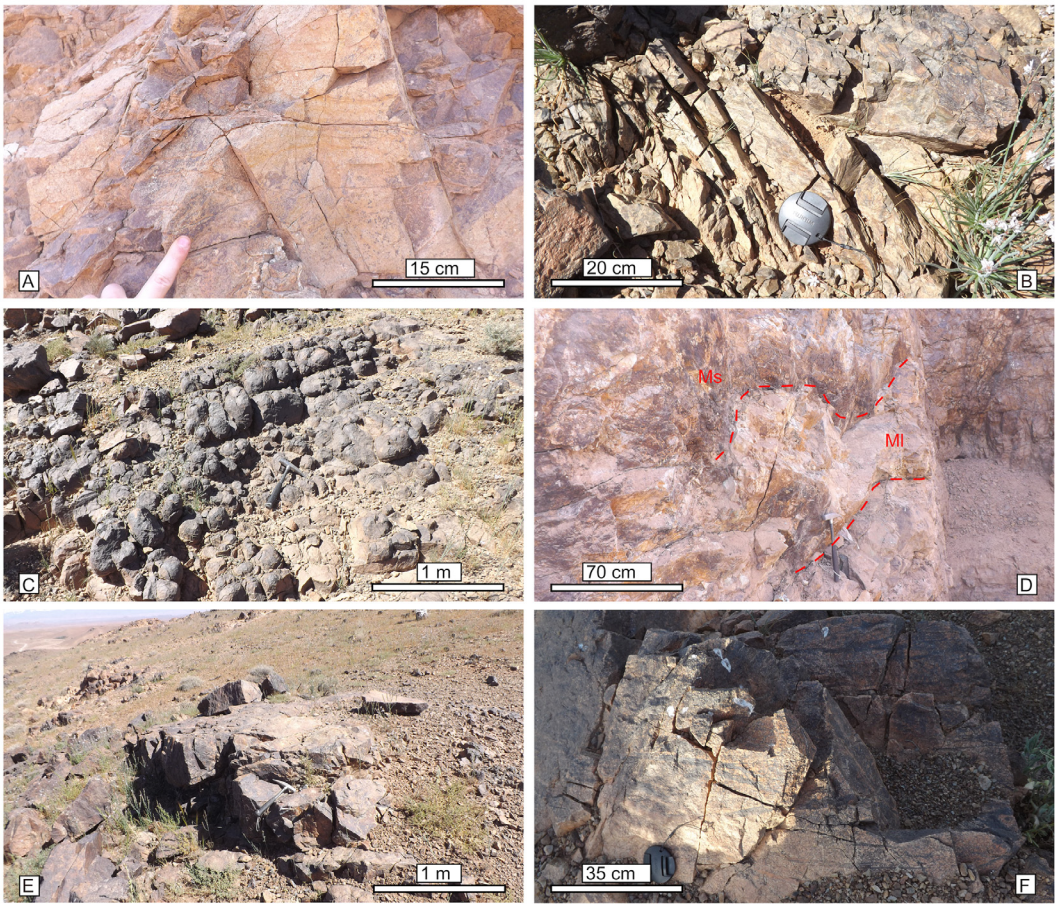

Fig. 14. (a) Parallel laminated metasandstone of Aït Witfao Fm. (b) Metapelite of Aït Witfao Fm. (c) Pillow-lava structures, indicating underwater extrusion, interbedded in the metasiliciclastic sediment of the Aït Witfao Fm. (d) Metalimestone (Ml) interbedded in metasandstone (Ms) of Aït Witfao Fm. (e) Metachert or jaspers interbedded in the metapelite of Aït Witfao Fm. (f) Ediacaran granodioritic dike which intruded the Cryogenian metasedimentary rocks.

by low resistivity values, from the host rock generally characterized by high values of electrical resistivity.

Our study, based on a multidisciplinary approach, consisted in extensive ERT survey accompanied by geological fieldworks, petrographic and mineralogical studies, which allowed us to explore the Sidi Flah ore deposit, recognizing and reconstructing the setting of two different mineralized bodies, with a very low-cost and low-time-consuming method. Specifically, geological fieldworks and laboratory tests allowed us to distinguish two different mineralizations, one characterized by sphalerite/galena (zone "A") and one characterized by Fe, Cu-sulphides (zone "B"), impossible to explain only with geophysical survey.

As seen in synthetic resistivity models (Fig. 4), the DD configuration gives resistivity values lower at the bottom of the ERT models and produces sharper vertical border than WS; on the other hand, WS led to more realistic conductivity than DD which tends to overestimate the conductive body. Furthermore, the preliminary analysis on the three different quadripolar configurations, led us to proceed the ERT surveys using the DD and SR, because of approximately equal results obtained by SR and WS configurations.

Raw data acquired provided early a difference between the two quadripolar configurations, with in general Q factor for DD higher than SR. In Fig. 5 we compared results for the line *tomo_5_bis* among the three different configurations and it is clear the difference in terms of quality, where SR and WS show lower values of Q factor for repeated quadripoles measurements. As known for these configurations, the reason of more noisy data from DD configuration can be found in the lower strength of the signal for these configurations.

In terms of resistivity response, the DD showed extreme resistivity variations and in few cases chaotic results, probably affected from the variability of quadripolar measurements. Furthermore, RMSs for DD inverted model showed final values ranging from 4.3 to 27.6, which compared with the RMSs of SR (Figs. 11–13) can be an index of how variable and noisy are data acquired with DD.

Under considerations obtained from synthetic resistivity modelling and ERT results, according with our aim to individuate the more reliable configuration and for the capacity to give resistivity response similar to the geological settings, we chosen the SR as the best method to reveal and to interpret the mineralized bodies, for the studied area. The reliability of Schlumberger Reciprocal configuration was also demonstrated from Kumar et al. (2016) in sulphide mixed-ore deposits exploration.

As seen from mineralogic and petrographic analyses (§4.2), it is possible to distinguish two different main mineralizations, one consisting of mainly sphalerite and galena (Figs. 3a and 15c) and another consisting of Fe, Cu-sulphides (Figs. 3d and 15g). The reason for the higher electrical resistivity values of the zone "A" (sphalerite/galena mineralization) compared to zone "B" (Fe, Cu-sulphides mineralization) is due to the dominant composition of sphalerite and galena which have generally greater electrical resistivity values than those of Fe, Cu-sulphides. These electrical resistivity variations are in agreement with the literature data for mixed sulphides, where Fe, Cu-sulphides mineralizations usually have lower electrical resistivity values than sphalerite/galena mineralizations (e.g. Parasnis, 1956; Parkhomenko, 1967; Pridmore and Shuey, 1976; Carolyn et al., 2006; Pearce et al., 2006). Additionally, the zone "B" probably shows lower resistivity values and a larger conductive zone (Figs. 12 and 13) compared to the zone "A", also

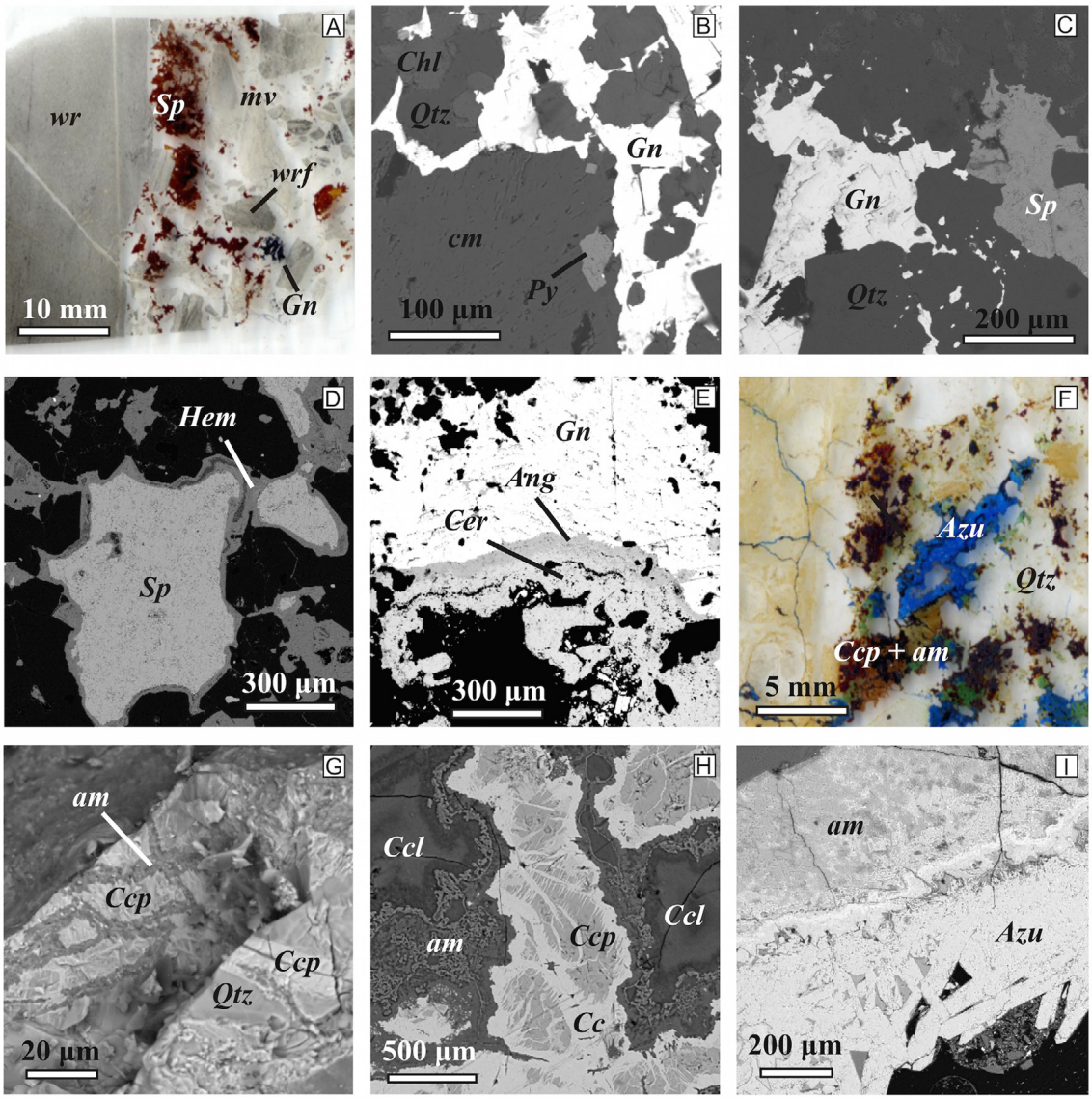

Fig. 15. Optic microscopy (parallel nicol) and SEM images of thin sections and fragments obtained by samples taken from sphalerite/galena mineralization (zone "A") (a-e) and from Fe, Cu-sulphides mineralization (zone "B") (f-i). (a) Optical image showing the mineralized vein of sphalerite/galena mineralization (zone "A") in contact with the metapelitic wall rock. The vein contains quartz and carbonatic gangue hosting mainly sphalerite and galena. Fragments of the wall rock are commonly found inside the vein. (b) Backscattered SEM image of a galena domain, neighbouring smaller pyrite and chlorite domains. (c) Backscattered SEM image of a galena domain and a sphalerite domain in close contact in the mineralized vein. (d) Backscattered SEM image showing hemimorphite alteration of sphalerite. (e) Backscattered SEM image showing anglesite and cerussite alteration halos on galena. (f) Optical image showing a mineralized vein of Fe, Cu-sulphides mineralization (zone "B"). The quartz gangue hosts bluish, greenish and brownish areas, mainly populated by alteration minerals. (g) Secondary SEM image of a fragment of the mineralized vein, showing chalcopyrite domains surrounded by alteration minerals. (h) Backscattered SEM image of altered chalcopyrite domains. (i) Backscattered SEM image of an area close to a geode (dark area in image) surrounded by millimetres prismatic azurite crystals and a halo of mixed alteration minerals. Abbreviations: am: mixed alteration minerals (mainly sulphates, arsenates, carbonates and hydroxides of Cu, Fe, Sb, Ni, Mn, Ca, Co and Mg); cm: mixed carbonate minerals (calcite, dolomite and ankerite); mv: mineralized vein; wr: wall rock; wrf: wall rock fragment; Ang: anglesite; Azu: azurite; Cc: chalcocite; Ccl: chrysocolla; Ccp: chalcopyrite; Cer: cerussite; Chl: chlorite; Gn: galena; Hem: hemimorphite; Qtz: quartz; Py: pyrite; Sp: sphalerite.

due to the greater diffusion of chalcopyrite and its alteration minerals (Figs. 3d, 15f and 15i) into the host rocks.

As seen in Figs. 11–13, the zone "A" shows a variation of electrical resistivity with the tendency to decrease toward the northern part of the Sidi Flah mine. Furthermore, there are local portion of the "Area 1", in the southern part of Sidi Flah mining area, where the conductive body defined as zone "A" disappear, as showed in the lines *tomo_4* and *tomo_4_bis* (Fig. 11). This is probably due to the irregular dimensions of the mineralized dyke, with local drastically reduction of thickness. The geological information which derived from the mining trench and pits, can confirm the hypothesis that the local mineralized veins are very thin.

At the top of the morphological relief on the east side of the studied area, between *tomo_05_bis* and *tomo_09*, there is a high and localized increment of electrical resistivity above the Fe, Cu-sulphide mineralization (zone "B") (Figs. 12 and 13), which starts from the terrain surface and reaches the maximum depth of about 6 m. This zone (zone "D") appears as a discordance respect to the below conductive body (zone "B") and it can be explained as the result of leaching process occurred to the mineralized body. Moreover, the presence of many secondary mineral phases (Figs. 3d, 15f and 15i) can be considered a confirmation of the leaching process suffered by the Fe, Cu-sulphide mineralization. In fact, this phenomenon disappears at minor topographic elevation in direction of the depocentre of the valley and inside

the mining pits.

In the "Area 1" and "Area 2", from *tomo_1* to *tomo_7* (and partially *tomo_10*), it is possible to see a sub-horizontal conductive body (< 100 Ω*m.) with variable thickness up to 10 m (zone "C"). In these resistivity models, this anomaly is located in the depocentre of the valley, characterized prevalently by alluvial and mining dump deposits (Figs. 11 and 12). This result can be an outcome of the alteration and deposition process of metallic minerals due to the past water runoff and partially due to the store of excavation products rich in conductive minerals (e.g. Fe, Cu-sulphides). Similar results were obtained by Mele et al. (2013) on mining dump deposits which containing fragments of mineralization (mainly pyrite and hematite) and barren rocks, and are characterized by low resistivity values (< 50 Ω*m) compared to the surrounding metamorphic bedrock.

With the above considerations, the ERT results show variations in electrical resistivity substantially connected with five specific zones:

- A: sphalerite/galena mineralization characterized by electrical resistivity values between 40 and 320 Ω*m.
- B: Fe, Cu-sulphides mineralization characterized by electrical resistivity values lower than 80 Ω*m.
- C: alluvial deposits and mining dump. This is also characterized by electrical resistivity values lower than 100 Ω*m, geomorphologically placed into the valley with maximum depth ca.10 m.
- D: leaching zone. In the ERT models, the leaching zone is located above the mineralized bodies, from ground level to a maximum depth of about 6 m, and show electrical resistivity values greater than 300 Ω*m.
- E: host rock. Includes all types of rocks described in §4.2.1 and are characterized by resistivity values greater than 150 Ω*m.

More quantitative considerations could be added by comparing ERT results with synthetic resistivity modelling.

The ERT method allowed us to individuate the mineralized portions, giving conductive areas larger than the real thickness of the mineralization. Moreover, the resistivity variation of zone "A" along all ERT models, from south to north of the studied area, can be considered also as an indicator of thickness variation, in agreement with geological setting of mineralized body.

6. Conclusion

Several 2D high-resolution ERT models have been acquired and interpreted in the Sidi Flah mine. Rarely utilized alone to explore mixed sulphides mineralization, ERT in this case showed mineralized portions as low resistivity anomalies in conjunction with ore mixed-sulphide settings. In general, the ERT, constrained with information provided from geological fieldworks and laboratory tests (petrographical and mineralogical analysis), allowed us to confirm the presence of mineralized volumes (characterized by low resistivity values) and localize with good resolution the main ore bodies. Another crucial result is the possibility to distinguish different mineralizations based on their resistivity values and petrographical/mineralogical evidences.

The SR configuration allowed us to carry out the survey with a good vertical and lateral resolution with a better data quality respect to the DD configuration, probably due to a higher signal intensity.

A drawback intrinsic of the ERT on which we focused has been the electrodic step. The spacing of the array is strictly related to the dyke dimension and the depth of investigation and, as seen in real and synthetic resistivity models, it can affect resistivity values and their resolution. This is the main reason which led us to acquire few lines with both 2 and 3 m electrodic step, to have an adequate resolution and to reach greater exploration depth.

We consider this kind of approach very useful for studying shallow and thin ore deposits also in presence of considerable resistivity contrast respect to the hosting rocks. The most critical limit of this approach is the difficulty in the estimation of the real vein dimensions, because only a relative variation of the thickness within the studied area can be obtained. However, we consider this approach a useful method to delineate the geological setting of mixed sulphides mineralization and valid as exploration survey to plan borehole tests.

Acknowledgements

The authors wish to thank M. Kouari for fruitful discussion about the ore deposits of Anti-Atlas belt, T. Colonna and CGT Group for the logistic and technical support, L. Carmignani for the discussion and interpretation of the ERT models and C. Viti and G. Giorgetti for helping with SEM measurements. Two anonymous reviewer are thanked for providing useful comments and suggestions that greatly improved the original submitted paper.

References

Abia, E.H., Nachit, H., Ibhi, H., Baroudi, Z., 1999. Les minéralisations filoniennes à Pb, Zn et Cu de la boutonnière de l'Ougnat, relations avec les déformations et essai de calage chronologique. Chron. Rech. Min. 536 (537), 137–149.

Abia, E.H., Nachit, H., Marignac, C., Ibhi, A., Aït Saadi, S., 2003. The polymetallic Au-Ag bearing veins of Bou Madine (Jbel Ougnat, eastern Anti-Atlas, Morocco): tectonic control and evolution of a Neoproterozoic epithermal deposit. J. Afr. Earth Sci. 36, 251–271. https://doi.org/10.1016/S0899-5362(03)00051-4.

Admou, H., Samson, S., Essaifi, A., Wafika, A., 2002. A new datation at 760 Ma of the plagiogranites associated to the Neo-proterozoic Bou Azzer and Siroua ophiolite (Anti-Atlas, Morocco). In: Nineteenth Colloquium of African Geology, El Jadida, Morocco, Abstr. vol. 4–5.

Aït Malek, H., Gasquet, D., Bertrand, J.M., Leterrier, J., 1998. Géochronologie U-Pb sur zircon de granitoïdes éburnéens et panafricains dans les boutonniéres protérozoïques d'Igherm, du Kerdous et du Bas Draa (Anti-Atlas occidental, Maroc). C. R. Acad. Sci. Paris Sci. Terre et Planets, pp. 819–826 10.1016/S1251-8050(99)80056-1.

Alilou, S.K., Norouzi, G.H., Doulati, F., Abedi, M., 2014. Application of magnetometry, electrical resistivity and induced polarization for exploration of poly-metal deposits, a case study: Halab Dandi, Zanjan, Iran. In: 2nd Intl' Conference on Advances in Engineering Sciences and Applied Mathematics (ICAESAM 2014) May 4–5, 2014. Istanbul, Turkey.

Barodi, E.B., Maacha, L., Zinbi, Y., 1998. Les minéralisations argentiféres au Maroc: cas du gisement d'Imiter. Chron. Rech. Min. 531 (532), 77–92.

Benssaou, M., Hamoumi, N., 1999. Palèoenvironnements et minéralisations de l'Anti-Atlas occidental marocain au Cambrien précoce. Chron. Rech. Min. 536 (537), 113–120.

Benziane, F., Yazidi, A., Saadane, A., Yazidi, M., El Fahssi, A., Stone, B.D., Walsh, G.J., Burton, W.C., Aleinikoff, J.N., Ejjaouani, H., Kalai, M., 2008. Carte géologique au 1/50.000, Feuille Qal'at Mgouna. Notes et Mémoires du Service Géologique du Maroc. 468. p. 139.

Bertin, J., Loeb, J., 1976. Experimental and theoretical aspects of induced polarization, presentation and application of the IP method case histories. Geoexploration Monographs 1 (7). p. 250.

Bhattacharya, P.K., Patra, H.P., 1968. Direct Current Geoelectric Sounding, Principles and Interpretation, Methods in Geochemistry and Geophysics. Series-9. Elsevier Publishing Company.

Bouougri, E.H., 2003. The Moroccan Anti-Atlas: the West African Craton passive margin with limited Pan-African activity: implications for the northern limit of the craton: discussion. Precambrian Res. 120, 179–183.

Carolyn, I.P., Richard, A.D.P., Vaughan, J.D., 2006. Electrical and magnetic properties of sulfides. Rev. Mineral. Geochem. 61, 127–180. https://doi.org/10.2138/rmg.2006.61.3.

Charlot, R., 1976. The precambrian of the Anti-Atlas (Morocco). A geochronological synthesis. Precambrian Res. 3, 273–299. https://doi.org/10.1016/0301-9268(76)90013-9.

Cheilletz, A., Levresse, G., Gasquet, D., Azizi-Samir, M.R., Zyadi, R., Archibald, D.A., Farrar, E., 2002. The giant Imiter silver deposit: neoproterozoic epithermal mineralization in the Anti-Atlas, Morocco. Miner. Deposita 37, 772–781. https://doi.org/10.1007/s00126-002-0317-0.

Choubert, G., 1947. L'accident majeur de l'Anti-Atlas. Comptes Rendus Hebdomadaires des Seances de l'Academie des Sciences 224 (16). pp. 1172–1173.

Choubert, G., 1952. Histoire géologique du domaine de l'Anti-Atlas. Notes et Mémoires du Service Géologique du Maroc 100. p. 196.

Clauer, N., 1974. Utilisation de la méthode Rb-Sr pour la datation d'une schistosité de sédiments peu métamorphisés: application au Précambrien II de la boutonniére de Bou Azzer-El Graara (Anti-Atlas, Maroc). Earth Planet. Sci. Lett. 22, 404–412.

Dahlin, T., Leroux, V., Nissen, J., 2002. Measuring techniques in induced polarisation imaging. J. Appl. Geophys. 50 (3), 279–298. https://doi.org/10.1016/S0926-9851(02)00148-9.

Dahlin, T., Zhou, B., 2006. Multiple-gradient array measurements for multichannel 2D resistivity imaging. Near-Surf. Geophys. 4, 113–123. https://doi.org/10.3997/1873-0604.2005037.

De Groot-Hedlin, C., Constable, S., 1990. Occam's inversion to generate smooth, two-

dimensional models from magnetotelluric data. Geophysics 55 (12), 1613–1624. https://doi.org/10.1190/1.1442813.
Ducrot, J., 1979. Datation à 615 Ma de la granodiorite de Bleida et conséquences sur la chronologie des phases tectoniques, métamorphiques et magmatiques pan-africaines dans l'Anti-Atlas marocain. Bull. Soc. géol. France 7 (XXI), 495–499. https://doi.org/10.2113/gssgfbull.S7-XXI.4.495.
El Boukhari, A., Chaabane, A., Rocci, G., Tane, J.L., 1992. Upper Proterozoic ophiolites of the Siroua massif (Anti-Atlas, Morocco) a marginal sea and transform fault system. J. Afr. Earth Sci. 14, 67–80. https://doi.org/10.1016/0899-5362(92)90056-I.
Ennih, N., Liégeois, J.P., 2001. The Moroccan Anti-Atlas: the West African craton passive margin with limited Pan-African activity. Implications for the northern limit of the craton. Precambrian Res. 112, 289–302. https://doi.org/10.1016/S0301-9268(01)00195-4.
Ennih, N., Liégeois, J.P., 2008. The boundaries of the West African Craton, with special reference to the Basement of the Moroccan Metacratonic Anti-Atlas Belt. Geol. Soc. London 297, 1–17. https://doi.org/10.1144/SP297.1.
Evrad, M., Pirard, E., Nguyen, F., 2005. Geophysical Investigation of the Pb-Zn Deposit of Plombières, Belgium. In: 13th SGA Biennial meeting Nancy – France. Paper in scientific congress.
Ezzouhairi, H., 1997. Magmatisme et tectonique de l'arc Precambrien de Bouskour (Saghro occidental, Anti-Atlas, Maroc). Comunicacones do Instituto Geologico e Mineiro 83, 47–52.
Fekkak, A., Pouclet, A., Ouguir, H., Badra, L., Gasquet, D., 1999. Le groupe du Néoprotérozoïque inférieur de Kelaat Mgouna (Saghro, Anti-Atlas, Maroc): témoin d'un stade précoce de l'extension pré-panafricaine. Bull. Soc. Géol. France 170 (6), 789–797.
Fekkak, A., Boualoul, M., Badra, L., Amenzou, M., Saquaque, A., El Amrani, I.E., 2000. Origine et contexte géotectonique des dépôts détritiques du groupe néoprotérozoïque inférieur de Kelaat Mgouna (Anti-Atlas oriental, Maroc). J. Afr. Earth Sci. 30 (2), 295–311. https://doi.org/10.1016/S0899-5362(00)00021-X.
Fekkak, A., Pouclet, A., Ouguir, H., Ouazzani, H., Badra, L., Gasquet, D., 2001. Géochimie et signification géotectonique des volcanites du Cryogénien inférieur du Saghro (Anti-Atlas oriental, Maroc). Geodin. Acta 14, 373–385. https://doi.org/10.1080/09853111.2001.10510730.
Fekkak, A., Pouclet, A., Badra, L., 2002. The Pre-Pan-African rifting of Saghro (Anti-Atlas, Morocco): example of the middle Neoproterozoic Basin of Boumalne. Bull. Soc. Géol. France 173 (1), 25–35. https://doi.org/10.2113/173.1.25.
Fekkak, A., Pouclet, A., Benharref, M., 2003. The Middle Neoproterozoic Sidi Flah Group (Anti-Atlas, Morocco): synrift deposition in a Pan-African continent/ocean transition zone. J. Afr. Earth Sci. 37, 73–87. https://doi.org/10.1016/S0899-5362(03)00049-6.
Gasquet, D., Levresse, G., Cheilletz, A., Azizi-Samir, M.R., Mouttaqi, A., 2005. Contribution to a geodynamic reconstruction of the Anti-Atlas (Morocco) during Pan-African times with the emphasis on inversion tectonics and metallogenic activity at the Precambrian-Cambrian transition. Precambrian Res. 140, 157–182. https://doi.org/10.1016/j.precamres.2005.06.009.
Gasquet, D., Ennih, N., Liégeois, J.P., Soulaimani, A., Michard, A., 2008. The Pan-African belt. Chapter 2 In: Michard, A., Saddiqi, O., Chalouan, A., Frizon de Lamotte, D. (Eds.), Continental Evolution: The Geology of Morocco. Lecture Notes in Earth Sciences 116. Springer-Verlag, Berlin Heidelberg, pp. 33–64. https://doi.org/10.1007/978-3-540-77076-3_2.
Grant, F.S., West, G.F., 1965. Interpretation Theory in a Applied Geophysics. McGraw Hill Book Company.
Harrison, R.W., Yazidi, A., Benziane, F., Quick, J.E., El Fahssi, A., Stone, B.D., Yazidi, M., Saadane, A., Walsh, G.J., Aleinikoff, J.N., Ejjaouani, H., Kalai, M., 2008. Carte géologique au 1/50.000, Feuille Tizgui. Notes et Mémoires du Service Géologique du Maroc 470, p. 131.
Hefferan, K.P., Admou, H., Karson, J.A., Saquaque, A., 2000. Anti-Atlas (Morocco) role in Neoproterozoic western Gondwana reconstruction. Precambrian Res. 103, 89–96. https://doi.org/10.1016/S0301-9268(00)00078-4.
Hefferan, K.P., Admou, H., Hilal, R., Karson, J.A., Saquaque, A., Juteau, T., Bohn, M.M., Samson, S.D., Kornprobst, J.M., 2002. Proterozoic blueschist-bearing melange in the Anti-Atlas Mountains, Morocco. Precambrian Res. 118, 179–194. https://doi.org/10.1016/S0301-9268(02)00109-2.
Hindermeyer, J., Gauthier, H., Destombes, J., Choubert, G., Faure-Muret, A., Laville, E., Lesage, J.L., du Dresnay, R., 1977. Carte géologique au 1/200.000, Jebel Saghro-Dadès (Haut Atlas central, sillon Sud-Atlasique et Anti-Atlas oriental). Notes et Mémoires du Service Géologique du Maroc, p. 161.
Ighid, L., Saquaque, A., Reuber, I., 1989. Plutons syn-cinematiques et la deformation panafricaine majeure dans le Saghro oriental (boutonniere d'Imiter, Anti-Atlas, Maroc). Comptes Rendus de l'Academie des Sciences, Serie 2, Mecanique, Physique, Chimie, Sciences de l'Univers. Sci. de la Terre 309 (6), 615–620.
IRIS Instruments, 2003. SYSCAL-Pro standard & switch (48-72 or 96) version. User's manual. p. 66.
Jochymczyk, K., Cabala, J., Poreba, A., 2006. Application of resistivity imaging to recognition of geological structure in the area of shallow Zn-Pb ore bodies (preliminary study). Acta Geodyn. Geomater. 3 (143), 131–138.
Kemna, A., Binley, A., Ramirez, A., Daily, W., 2000. Complex resistivity tomography for environmental applications. Chem. Eng. J. 77, 11–18. https://doi.org/10.1016/S1385-8947(99)00135-7.
Kneisel, C., 2006. Assessment of subsurface lithology in mountain environments using 2D resistivity imaging. Geomorphology 80 (1–2), 32–44. https://doi.org/10.1016/j.geomorph.2005.09.012.
Knoll, A.H., 2000. Learning to tell Neoproterozoic time. Precambr. Res. 100, 3–20. https://doi.org/10.1016/S0301-9268(99)00067-4.
Koefoed, O., 1979. Geosounding Principles 1: Resistivity Sounding Measurements. Elsevier Scientific Publishing Company, pp. pp.
Kumar, D., Subba Rao, D.V., Sridhar, K., Satyanarayanan, M., Patro, P.K., 2016. Integrated geophysical and geological studies for mineral prospecting in Betul-Chhindwara Belt (BCB), Central India. J. Geol. Soc. India 87, 383–396. https://doi.org/10.1007/s12594-016-0406-9.
Leblanc, M., Lancelot, Y., 1980. Interprétation géodynamique du domaine pan-africain (Précambrien terminal) de l'Anti-Atlas (Maroc) à partir de données géologiques et géchronologiques. Can. J. Earth Sci. 17, 142–155. https://doi.org/10.1139/e80-012.
Lecolle, M., Derre, C., Benkirane, Y., Nerci, K., 1989. Lithostratigraphie, tectonique et magmatisme des substratums des boutonnières de Sidi Flah-Bou Skour et de Boumalne du Dadès (Saghro, Anti-Atlas oriental, Maroc); consequences sur l'âgedes séries constitutives. Sciences Geologiques Memoire 83, 27–46.
Lecolle, M., Derré, C., Rjimati, E., Nerci, K., Azza, A., Bennani, A., 1991a. Les distensions et la tectonique biphasée du Panafricain de l'Anti-Atlas oriental: dynamique de dépôt et de structuration des Précambriens II-2 et II-3 (Saghro, Maroc). C. R. Acad. Sci. Paris 313 (II), 1563–1568.
Lecolle, M., Derré, C., Nerci, K., 1991b. The Proterozoic sulphide alteration pipe of Sidi Flah and its host series; new data for the geotectonic evolution of the Pan African Belt in the eastern Anti-Atlas (Morocco). Ore Geol. Rev. 6 (6), 501–536. https://doi.org/10.1016/0169-1368(91)90045-9.
Legault, J.M., Carriere, D., Petrie, L., 2008. Synthetic model testing and distributed acquisition dc resistivity results over an unconformity uranium target from the Athabasca Basin, northern Saskatchewan. Lead. Edge 27 (1), 46–51. https://doi.org/10.1190/1.2831679.
Loke, M.H., 2012. Tutorial: 2-D and 3-D Electrical Imaging Surveys. GeoTomo Software, Malaysia, pp. 168.
Loke, M.H., Chambers, J.E., Rucker, D.F., Kuras, O., Wilkinson, P.B., 2013. Recent developments in the direct-current geoelectrical imaging method. J. Appl. Geophys. 95, 135–156. https://doi.org/10.1016/j.jappgeo.2013.02.017.
Magnusson, M.K., Fernlund, J.M.R., Dahlin, T., 2010. Geoelectrical imaging in the interpretation of geological conditions affecting quarry operations. B. Eng. Geol. Environ. 69 (3), 465–486. https://doi.org/10.1007/s10064-010-0286-y.
Malusà, M.G., Polino, R., Cerrina Feroni, A., Ellero, A., Ottria, G., Baidder, L., Musumeci, G., 2007. Post-Variscan tectonics in eastern Anti-Atlas (Morocco). Terra Nova 19 (6), 481–489. https://doi.org/10.1111/j.1365-3121.2007.00775.x.
Massironi, M., Bertoldi, L., Calafa, P., Visonà, D., Bistacchi, A., Giardino, C., Schiavo, A., 2008. Interpretation and processing of ASTER data for geological mapping and granitoids detection in the Saghro massif (eastern Anti-Atlas, Morocco). Geosphere 4 (4), 736–759. https://doi.org/10.1130/GES00161.1.
Mele, M., Servida, D., Lupis, D., 2013. Characterisation of sulphide-bearing waste-rock dumps using electrical resistivity imaging: the case study of the Rio Marina mining district (Elba Island, Italy). Environ. Moint. Assess. 185 (7), 5891–5907. https://doi.org/10.1007/s10661-012-2993-2.
Michard, A., Frizon de Lamotte, D., Saddiqi, O., Chalouan, A., 2008. An outline of the geology of Morocco. Chapter 1 In: Michard, A., Saddiqi, O., Chaloua, A., Frizon de Lamotte, D. (Eds.), Continental Evolution: The Geology of Morocco. Lecture Notes in Earth Sciences 116. Springer-Verlag, Berlin Heidelberg, pp. 1–31. https://doi.org/10.1007/978-3-540-77076-3_1.
Moreira, C.A., Montenegro Lapola, M., Carrara, A., 2016. Comparative analyzes among electrical resistivity tomography arrays in the characterization of flow structure in free aquifer. Geofísica Internacional 55 (2), 119–129.
Morgan, L.A., 2012. Geophysical characteristics of volcanogenic massive sulfide deposits in volcanogenic massive sulfide occurrence model. U.S. Geological Survey Scientific Investigations Report, Chapter 7, 2010-5070.
Nance, R.D., Murphy, J.B., Strachan, R.A., Keppie, J.D., Gutiérrez-Alonso, G., Fernández-Suárez, J., Quesada, C., Linnemann, U., D'Lemos, R., Pisarevsky, S.A., 2008. Neoproterozoic-early Palaeozoic tectonostratigraphy and palaeogeography of the Peri-Gondwanan Terranes: Amazonian vs West African Connections. Geol. Soc. of London 297, 345–383. https://doi.org/10.1144/SP297.17.
Nelson, P.H., Van Voorhis, G.D., 1983. Estimation of sulfide content from induced polarization data. Geophysics 48 (1), 62–75. https://doi.org/10.1190/1.1441408.
Okpoli, C.C., 2013. Sensitivity and resolution capacity of Electrode configurations. Int. J. Geophys. 2013, 1–12. https://doi.org/10.1155/2013/608037.
Ouguir, H., Macaudiére, J., Dagallier, G., 1996. Le Protérozoïque supérieur d'Imiter (Saghro oriental, Maroc): un contexte géodynamique d'arriére-arc. J. Afr. Earth Sci. 22, 173–189. https://doi.org/10.1016/0899-5362(96)00002-4.
Parasnis, D.S., 1956. The electrical resistivity of some sulphide and oxide minerals and their ores. Geophys. Prospect. 4, 249–279. https://doi.org/10.1111/j.1365-2478.1956.tb01409.x.
Parasnis, D.S., 1986. Principles of Applied Geophysics, fourth ed. Chapman and Hall, London, UK, pp. 402.
Parkhomenko, E.I., 1967. Electrical Properties of Rocks. Plenum Press, New York, pp. 313.
Pearce, C.I., Pattrick, R.A.D., Vaughan, D.J., 2006. Electrical and magnetic properties of sulphides. Rev. Mineral. Geochem. 61, 127–180. https://doi.org/10.2138/rmg.2006.61.3.
Pridmore, D.F., Shuey, R.T., 1976. The electrical resistivity of galena, pyrite, and chalcopyrite. Am. Mineral. 61, 248–259.
Rezeau, H., Chelle-Michou, C., Calder, M., 2014. Geology and Metallogeny of the Atlas Mountains, Morocco. Excursion guide, 29 March-7April 2014. University of Geneva, Switzerland, and Montpellier, France, pp. 77.
Saadane, A., 2004. Le batholithe composite de Saghro (Anti-Atlas Oriental, Maroc). Notes et Mémoires du Service Géologique du Maroc 464. p. 194.
Saquaque, A., Admou, H., Karson, J.A., Hefferan, J., Reuber, I., 1989. Precambrian accretionary tectonics in the Bou Azzer-El Graara region, Anti-Atlas, Morocco. Geology 17, 1107–1110. https://doi.org/10.1130/0091-7613(1989) 017<1107:PATITB>2.3.CO;2.

Saquaque, A., Benharref, M., Abia, H., Mrini, Z., Reuber, I., Karson, J.A., 1992. Evidence for a Panafrican volcanic arc and wrench faults tectonics in the Jbel Saghro, Anti-Atlas, Morocco. Geol. Rundsch. 81, 297–309. https://doi.org/10.1007/BF01764536.

Sasaky, Y., 1992. Resolution of resistivity tomography inferred from numerical simulation. Geophys. Prospect. 40 (4), 453–463. https://doi.org/10.1111/j.1365-2478.1992.tb00536.x.

Shermerhorn, L.G.G., Wallberecher, E., Huch, K.M., 1986. Der subduktions komplex, granit plutonismus und schertektonik im grundgebirge des Sirwa-doms (Anti-Atlas, Marokko). Berliner Geowiss. Abh. 66, 301–322.

Stone, B.D., Benziane, F., El Fahssi, A., Yazidi, A., Walsh, G.J., Yazidi, M., Saadane, A., Ejjaouani, H., Kalai, M., 2008. Carte géologique au 1/50.000, Feuille Sidi Flah. Notes et Mémoires du Service Géologique du Maroc 467. p. 114.

Sumner, J.S., 1976. Principles of Induced Polarization for Geophysical Exploration. Elsevier Publication, pp. 277.

Tavakoli, S., Elming, S.Å., Thunehed, H., 2012. Geophysical modelling of the central Skellefte district, Northern Sweden; an integrated model based on the electrical, potential field and petrophysical data. J. Appl. Geophys. 82, 84–100. https://doi.org/10.1016/j.jappgeo.2012.02.006.

Tavakoli, S., Bauer, T.E., Rasmussen, T.M., Weihed, P., Elming, S.Å., 2016. Deep massive sulphide exploration using 2D and 3D geoelectrical and induced polarization data in Skellefte mining district, northern Sweden. Geophys. Prospect. 1–8. https://doi.org/10.1111/1365-2478.12363.

Thomas, R.J., Chevallier, L.P., Gresse, P.G., Harmer, R.E., Eglington, B.M., Armstrong, R.A., de Beer, C.H., Martini, J.E.J., de Kock, G.S., Macey, P.H., Ingram, B.A., 2002. Precambrian evolution of the Sirwa Window, Anti-Atlas Orogen, Morocco. Precambrian Res. 118, 1–57. https://doi.org/10.1016/S0301-9268(02)00075-X.

Thomas, R.J., Fekkak, A., Ennih, N., Errami, E., Loughlin, S.C., Gresse, P.G., Chevallier, L.P., Liégeois, J.P., 2004. A new lithostratigraphic framework for the Anti-Atlas Orogen, Morocco. J. Afr. Earth Sci. 39, 217–226. https://doi.org/10.1016/j.jafrearsci.2004.07.046.

Tuduri, J., Chauvet, A., Ennaciric, A., Barbansona, L., 2005. Modèle de formation du gisment d'argent d'Imiter (Anti-Atlas oriental, Maroc). Nouveaux apports de l'analyse structural et minéralogique. C. R. Geosci. 338, 253–261. https://doi.org/10.1016/j.crte.2005.11.010.

Villeneuve, M., Cornée, J.J., 1994. Structure, evolution and palaeogeography of the West African Craton and bordering belts during the Neoproterozoic. Precambrian Res. 69, 307–326. https://doi.org/10.1016/0301-9268(94)90094-9.

Walsh, G.J., Aleinikoff, J.N., Benziane, F., Yazidi, A., Armstrong, T.R., 2002. U-Pb zircon geochronology of the Paleoproterozoic Tagragra de Tata inlier and its Neoproterozoic cover, western Anti-Atlas, Morocco. Precambrian Res. 117, 1–20. https://doi.org/10.1016/S0301-9268(02)00044-X.

Walsh, G.J., Yazidi, A., Benziane, F., Burton, W.C., El Fahssi, A., Stone, B.D., Yazidi, M., Saadane, A., Aleinikoff, J.N., Ejjaouani, H., Kalai, M., 2008a. Carte géologique au 1/50.000, Feuille Timdghas. Notes et Mémoires du Service Géologique du Maroc 471. p. 107.

Walsh, G.J., Benziane, F., Burton, W.C., El Fahssi, A., Yazidi, A., Yazidi, M., Saadane, A., Aleinikoff, J.N., Ejjaouani, H., Harrison, R.W., Stone, B.D., Kalai, M., 2008b. Carte géologique au 1/50.000, Feuille Bouskour. Notes et Mémoires du Service Géologique du Maroc. 469, p. 131.

Walsh, G.J., Benziane, F., Aleinikoff, J.N., Harrison, R.W., Yazidi, A., Burton, W., Quick, J.E., Saadane, A., 2012. Neoproterozoic tectonic evolution of the Jebel Saghro and Bou Azzer-El Graaran inliers, eastern and central Anti-Atlas, Morocco. Precambrian Res. 216 (219), 23–62. https://doi.org/10.1016/j.precamres.2012.06.010.

Wong, J., Strangway, D.W., 1981. Induced polarization in disseminated sulfide ores containing elongated mineralization. Geophysics 46 (9), 1258–1268. https://doi.org/10.1190/1.1441264.

Yazidi, A., Benziane, F., Walsh, G.J., Harrison, R.W., Saadane, A., Yazidi, M., Quick, J.E., El Fahssi, A., Stone, B.D., Aleinikoff, J.N., Ejjaouani, H., Kalai, M., 2008. Carte géologique au 1/50.000, Feuille Ait Semgane. Notes et Mémoires du ServiceGéologique du Maroc. 472. p. 113.